Design and Optimization of a Stacked Three-Layer X-ray Detector for Multi-Spectral Medical Imaging Applications

by

Sebastian Lopez Maurino

A thesis
presented to the University of Waterloo
in fulfillment of the
thesis requirement for the degree of
Master of Applied Science
in
Electrical and Computer Engineering

Waterloo, Ontario, Canada, 2016

I hereby declare that I am the sole author of this thesis. This is a true copy of the thesis, including any required final revisions, as accepted by my examiners.

I understand that my thesis may be made electronically available to the public.

Abstract

Dual-Energy (DE) imaging is a powerful technique in x-ray imaging that increases the ability to detect specific materials in a cluttered background, and is used to more accurately visualize anatomical features and diagnose abnormalities. Single-shot imaging has arisen as one of the dominant techniques used to obtain DE images, but has the intrinsic drawback of a loss of x-ray photons in a metal mid-filter.

I propose a new design of a stacked three-layer x-ray detector for DE single-shot imaging that addresses this fundamental drawback. Each layer consists of its own scintillator of individual thickness and an underlying thin-film-transistor-based flat-panel. Three images are obtained simultaneously in the detector during the same x-ray exposure, and thus the imaging system is immune to motion artifacts. The detector operation is two-fold: a conventional radiography image can be obtained by combining all three layers' images, while a DE subtraction image can be captured from the front and back layers, where the middle layer acts as a filter that helps achieve spectral separation.

Two sample imaging tasks that can particularly benefit from this new detector design are selected. These are iodinated vessel visualization in coronary angiography and calcified nodule detection in pulmonary radiology. I proceed to optimize the detector parameters and imaging system configuration to best fit these two tasks by obtaining the best possible contrast to noise ratio per root entrance exposure. To achieve this, I develop an analytical model by adapting well-established theoretical foundations to fit this new detector design.

These results are compared to a conventional DE temporal subtraction detector and a typical single-shot DE subtraction detector with a metal mid-filter, both of which underwent a similar analytical optimization process. The findings are then validated using advanced Monte Carlo simulations for all optimized detector configurations.

The analytical and simulation results indicate that the proposed detector performs comparably as a DE imager to established single-shot detectors. It is therefore clear that this new design is an improvement on the state-of-the-art since it provides an additional feature at no performance cost.

Given the performance expected from these initial results and the recent decrease in price for digital x-ray detectors, the simplicity of the three-layer stacked imager approach appears promising to usher in a new generation of multi-spectral digital x-ray imaging.

Dedication

To my parents, Carlos and Marcela, for their infinite support.

Acknowledgements

Firstly, I would like to sincerely thank my supervisor, Dr. Karim S. Karim, for his guidance, help, and encouragement throughout my studies and the development of this project. I will always appreciate his ability to point me in new and exciting directions, and his patience to allow me to explore new possibilities.

Many thanks also go to my colleagues at the Silicon Thin-Film Applied Research (STAR) group, Abdallah El-Falou, Ahmet Camlica, Chris Scott, Hummer Li and Jerry Liang, for their friendship throughout my time here.

I am very appreciative of the help provided by Dr. Ian Cunningham with this project, particularly throughout its design stage. I am also much indebted to both Dr. Aldo Badano and Diksha Sharma from the FDA, for their assistance and guidance in performing Monte Carlo simulations.

Lastly, and perhaps most importantly, I would like to thank my family and friends for their continuous support; my parents and my brother, who always believed in me; and especially Kayla, who has proven to be an unlimited source of encouragement and inspiration.

Table of Contents

List of Tables

List of Figures

Chapter 1

Introduction

Ever since its conception, radiography has been used to study detailed human anatomies to aid in the diagnosis and treatment of diseases. Its contribution to the entire medical field has and will continue to be invaluable. The objective of these images is often to detect specific objects amongst a cluttered background formed from a superposition of normal anatomical tissue. Noise in this background can often obscure the objects of interest and make them impossible to detect.

A technique that has proven successful in removing background clutter and enhancing specific material content is Dual-Energy (DE) imaging. It does so by exploiting the difference in the degree in which body tissues attenuate high- and low-energy x-rays. This technique can be applied to a multitude of imaging tasks, where it can, for example, enhance vasculature in angiography or help detect calcifications in pulmonary radiography.

Applying DE techniques to obtain enhanced images requires a new x-ray imaging system capable of doing so. One of the main approaches to such systems that has emerged is that of single-shot DE imaging, which can simultaneously obtain a high- and low-energy image in two separate stacked sensitive detector layers. This thesis presents a new detector design for single-shot DE imaging systems that aims to improve on the state-of-the-art by the addition of a new detector feature without any added drawbacks.

To obtain two spectrally different images in each of its layers, conventional single-shot detectors make use of a metal mid-filter. While effective, the presence of this filter means that a portion of the incoming x-rays will be absorbed by it and therefore wasted. This

photon loss results in lower patient dose efficiency. To address this issue, my proposed detector design replaces the filter in conventional single-shot imagers by a third sensitive layer, making it a three-layer stacked detector. This new layer will simultaneously act as a beam-hardening filter and obtain its own image. Thanks to the recently decreasing costs of building flat-panel x-ray sensors, the addition of this layer could provide valuable information that was previously lost in the filter at little added financial cost and no added patient dose.

The purpose of this thesis is to evaluate the potential performance of this three-layer detector design as a DE imager. By comparing it to established single-shot detectors, it is possible to determine if the use of a sensitive layer in place of a metal filter leads to a comparable performance, and hence if the capturing of this previously-ignored information truly results in no image detriments. An analytical model is developed to calculate the quality of the images produces by such a detector, with which its optimal configuration is found. The results from this model are later validated using photon transfer Monte Carlo simulations.

Chapter 2

Background

2.1 X-rays, Their Generation and Their Interactions with Matter

X-rays are electromagnetic waves with wavelengths in the range of $0.01\,\mathrm{nm}$ to $10\,\mathrm{nm}$. Their ability to penetrate soft tissue and yet be efficiently absorbed in higher atomic number (Z) materials has allowed them to become an invaluable tool in medicine ever since their discovery over a century ago.

Radiography became the first medical imaging technology in the late 1800s when physicist Wilhelm Röentgen discovered x-rays and used them to take images of human anatomy. Radiography requires two critical components: an x-ray tube to generate x-rays, and a detector to capture them and form an image. Figure 2.1 shows the basic geometry in which these are placed around the patient in order to obtain a radiographic image. Unlike conventional photography where light bounces off the object being imaged, x-rays leave the source and go through the patient before reaching the detector. Due to variations in x-ray attenuation throughout the body, a two-dimensional image of the three-dimensional patient is created at the detector.

Applications of this technique are numerous in diagnostic and interventional medicine, as it is a non-invasive way to observe internal anatomies. This has allowed radiography to become an extremely common medical test and the most commonly used diagnostic medical imaging technique[1].
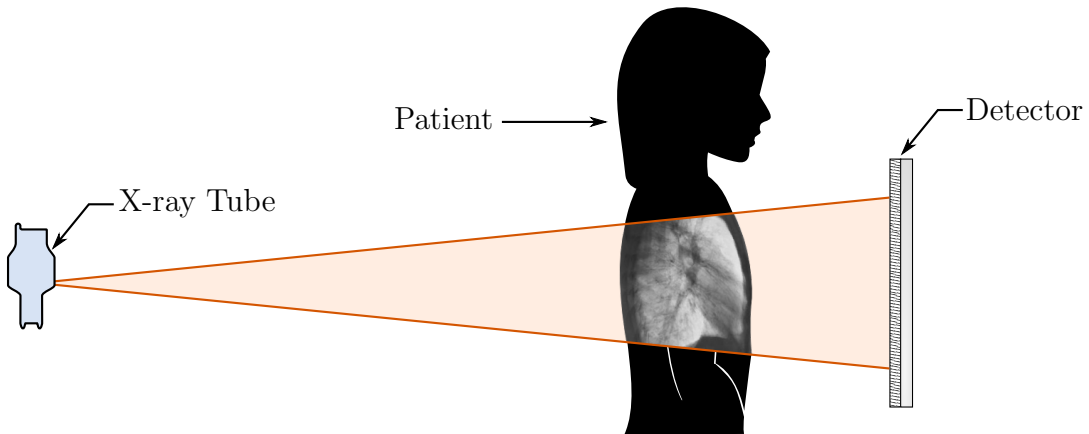
Figure 2.1: Illustration of the basic geometry of projection radiography. The x-ray beam generated in the tube goes through the patient, where it is preferentially absorbed in certain regions, allowing for the creation of an anatomical image at the detector.

2.1.1   X-ray Generation

Obtaining a radiographic image begins with the emission of a short-lived pulse of x-rays emitted by an x-ray tube. These tubes work by heating up a metal filament to a temperature where it will release free electrons. A high voltage referred to as the *tube voltage* is applied between it and a metal target, and thus a stream of electrons flows across the tube in what is known as the *tube current*. Due to interactions between the liberated electrons and the target, x-rays are produced in the latter and emerge in all directions (See Figure 2.2). In order to create a usefully-shaped beam, the x-rays are restricted in most directions by collimators. A glass envelope is used to maintain a vacuum around the entire system to avoid interactions between the electron beam and air molecules[2].

It is clear from this design that x-ray tubes are meant to operate at a single polarity of tube voltage, with the target acting as the anode and the filament as the cathode. However, the source of electrical power used in radiographic equipment is typically alternating current (AC). Furthermore, x-ray generation in the target is most efficient if the tube voltage is kept at a constant high value, while AC current will oscillate about zero. To get around these issues, most x-ray generation devices include full-wave rectifiers and use three-phase power to achieve a fairly constant positive tube voltage[3]. While some oscillations are still present, the tube voltage can be described with a single-valued property by referring to the
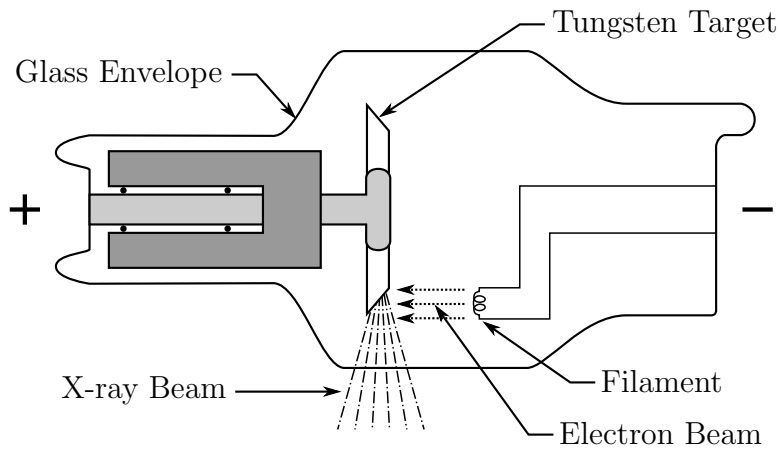
Figure 2.2: Diagram of the major components of a typical modern x-ray tube.

peak voltage of its oscillations[2]. This is referred to as the *peak tube voltage* and will be abbreviated henceforth as kVp (for kilo volts peak), since it is in units of kilo volts (kV).

Since the source of the energy of the produced x-rays will be the kinetic energy of the accelerated electrons hitting the target, it follows that the highest possible energy of said x-rays will be given by the peak tube potential. The unit of electronvolt (eV) is therefore very convenient, as the expected maximum x-ray energy in keV becomes the same as the tube potential in kV. (For example, a tube potential of 100 kV may generate x-rays with a maximum energy of 100 keV.) However, this method can only be used to determine the maximum value of a generated x-ray spectrum, and says little about its overall shape. The two effects that will additively contribute to and thus determine the energy distribution of the generated x-ray photons are Bremsstrahlung radiation and Characteristic radiation[4].

Bremsstrahlung

Bremsstrahlung—also called breaking radiation—occurs when the incoming electron interacts inelastically with an atom in the target. As the electron travels through the electromagnetic field of the atom, it loses only a portion of its kinetic energy and is deflected (see Figure 2.4). The transferred energy is released in the form of an x-ray photon, which can be of an energy as high as that of the original incoming electron[5]. This type of radiation will create a continuous spectrum throughout the entire energy range, as can be seen in Figure 2.3.
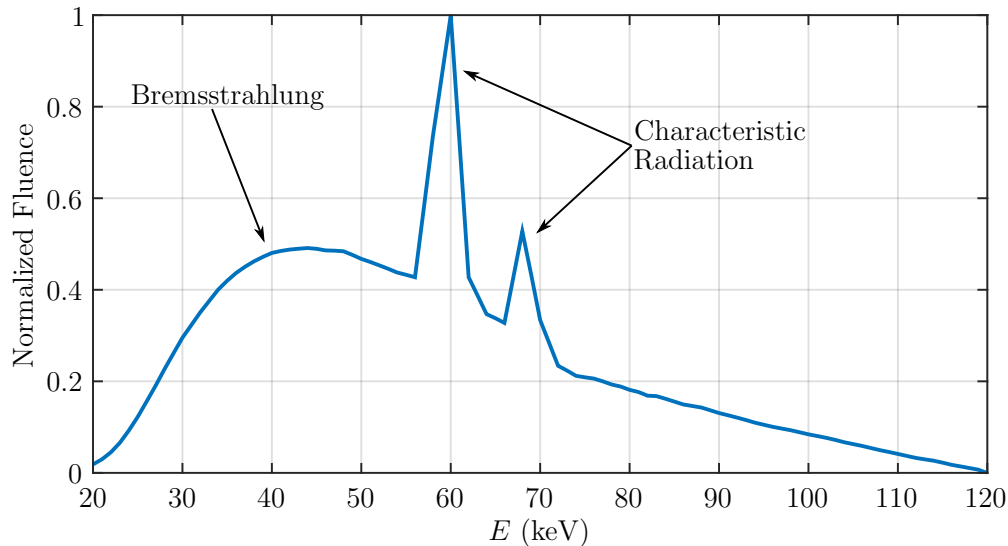
Figure 2.3: Contribution of both types of radiation to a typical x-ray spectrum emitted by a tungsten-anode tube at a kVp of 120 kV.

Characteristic Radiation

Electron transitions between atomic shells can result in fluorescent emission of x-ray photons. When an incoming electron from the filament knocks out one of the target atom's electrons into a higher shell, a vacancy is left behind. Immediately after, this vacancy is filled and a photon of energy equal to that of the difference between the binding energy of the two shells involved in this transition is emitted[6, 3]. Since the electron shell energies are discretized in nature, the photon emitted can only have one of a handful of energies. Radiation at these energies is named characteristic radiation, and the specific energies at which it occurs will depend on the material of the tube target.

2.1.2   X-rays Interaction with Matter

When an x-ray beam passes through matter, it will become weaker (i.e. its fluence will decrease) and is said to be *attenuated*. In the diagnostic x-ray energy range, this effect is due to three different types of interactions between x-rays and matter[5, 6], each of which

(a) Bremsstrahlung   **(b)** Characteristic Radiation
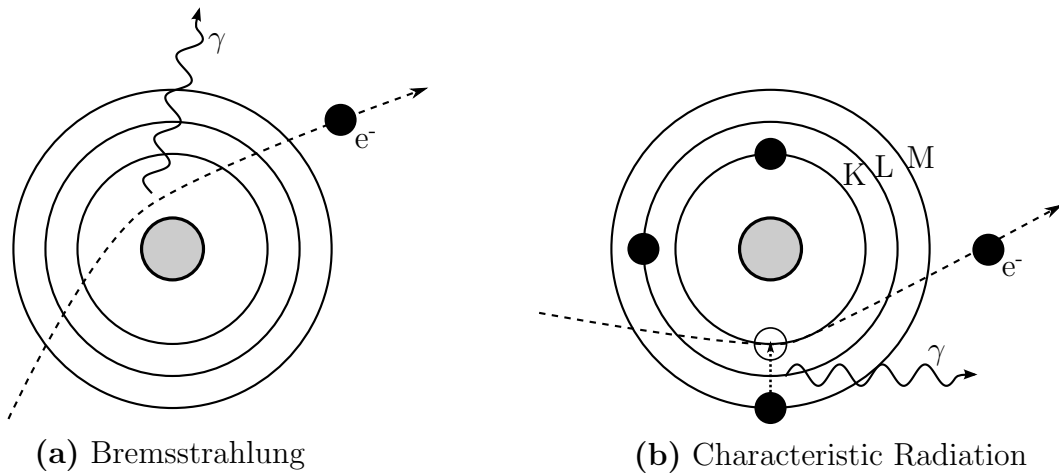
Figure 2.4: Simplified diagrams of electron-atom interactions that lead to x-ray radiation. **(a)** As the electron from the filament (e⁻) interacts with the atom, it loses kinetic energy that is liberated in the form of a photon (γ). **(b)** An atomic electron is kicked into a higher shell by the beam electron e⁻ and leaves a vacancy behind. When it proceeds to fill this vacancy, a photon γ is released.

are described in detail below. Figure 2.5 shows an example of the relative contributions of each of these processes to the total attenuation of x-rays passing through a material.

- **Rayleigh scattering** is the elastic interaction of the incoming photon with electrons through quantum resonance. While the x-ray loses no energy, its direction is changed. The probability of this event descreases with the photon energy, and thus will be most important for low-energy applications.

- **The photoelectric effect** is an absorption event in which all the energy of the photon is transferred to an electron that is ejected. Since the photon must posses more energy than the transition energy of one electron in order to eject it from its shell, the probability of photoelectric effect interactions will see a sudden jump once the photon energy passes any of these thresholds. The sharp edges appreciable in Figure 2.5 correspond to these transition energies. This effect will predominate the entire diagnostic x-ray range for all high-Z materials.

- **Compton scattering** occurs between a photon and a loosely bound electron. The electron is ejected from the atom, and the photon is scattered with a reduction in

its energy equal to the binding energy of the electron. The probability of this type of scatter increases with x-ray energy, and will in fact dominate at the upper end of the diagnostic range for low-Z materials, such as soft tissue.
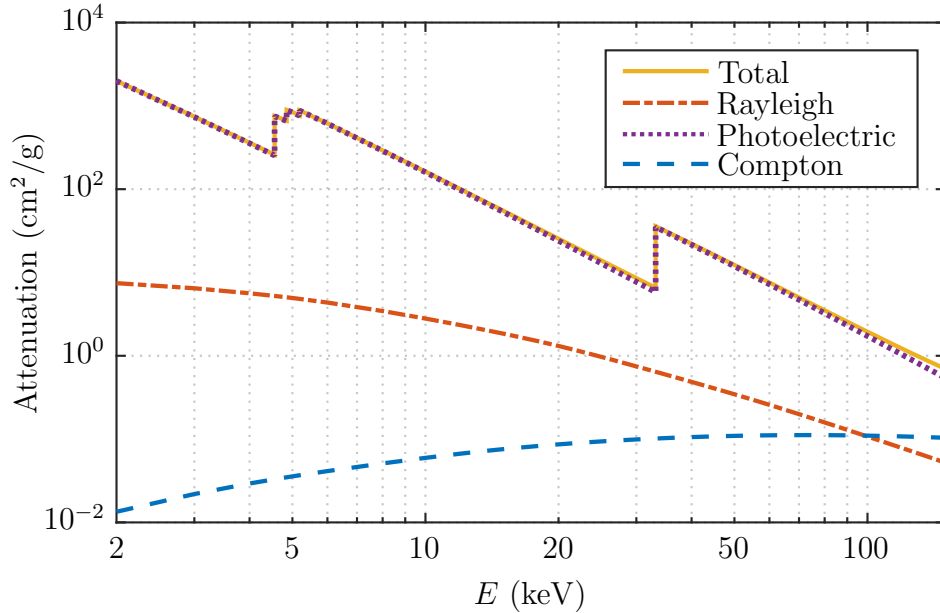
Figure 2.5: Contributions to x-ray attenuation of each photon-matter interaction mechanism in the diagnostic x-ray energy range for the common contrast agent iodine. Data obtained from [7].

2.1.3 Attenuation

The many effects that affect x-ray attenuation in matter can be hard to consider simultaneously. To easily perform quantitative calculations, we define the *linear attenuation coefficient*, μ, as the fractional attenuation of photons per unit length caused by all interaction processes. The intensity of an x-ray beam I that has penetrated a medium a distance z can then be then easily calculated using

$$I(z) = I_0 e^{-\mu z} \tag{2.1}$$

where I_0 is the initial intensity of the beam before reaching the medium. This equation is commonly known as the Beer-Lambert law and describes the exponential nature of electromagnetic attenuation in matter. The coefficient μ allows for such a simple mathematical expression since it is in fact the sum of the individual attenuation coefficient for each type of interaction:

$$\mu = \mu_{\text{Rayleigh}} + \mu_{\text{photoelectric effect}} + \mu_{\text{Compton scatter}}. \tag{2.2}$$

In the diagnostic x-ray range, μ will not be constant but will rather decrease as the photon energy increases (with the exception of sharp increments at the transition energies of the material). This energy dependence of μ ($\mu = \mu(E)$) will in fact play a very important role in the development of the three-layer detector presented here. Moreover, this phenomenon is also exploited to achieve a desired x-ray source filtration in specific applications.

Source Filtration

When passing through matter, the lower-energy photons of a polyenergetic x-ray beam will preferentially interact with the medium due to the energy dependence of μ[4, 3], and thus be removed from the beam. This shift to a beam that contains a higher proportion of high-energy photons than the original is dubbed *beam hardening*. Examples of said effect are shown in Figure 2.6, where it clear that additional filtration will preferentially affect the low-end of the spectrum. Radiography setups will typically include thin layers of aluminum, copper or other metalic materials as a filter placed immediately after the x-ray tube in order to achieve beam hardening. This source filtration practice is in place because the removal of low-energy x-rays will normally reduce the dose delivered to a patient and achieve higher-quality images.

2.2 Flat-Panel Detectors

The relatively recent addition of flat-panel detectors (FPDs) to x-ray systems has allowed for large-area and low-cost digital imaging[8]. Their Thin-Film-Transistor (TFT) technology is largely similar to that used in flat panel displays, whose recent surge in popularity has resulted in a significant cost reduction. Flat-panel TFT arrays are based on amorphous
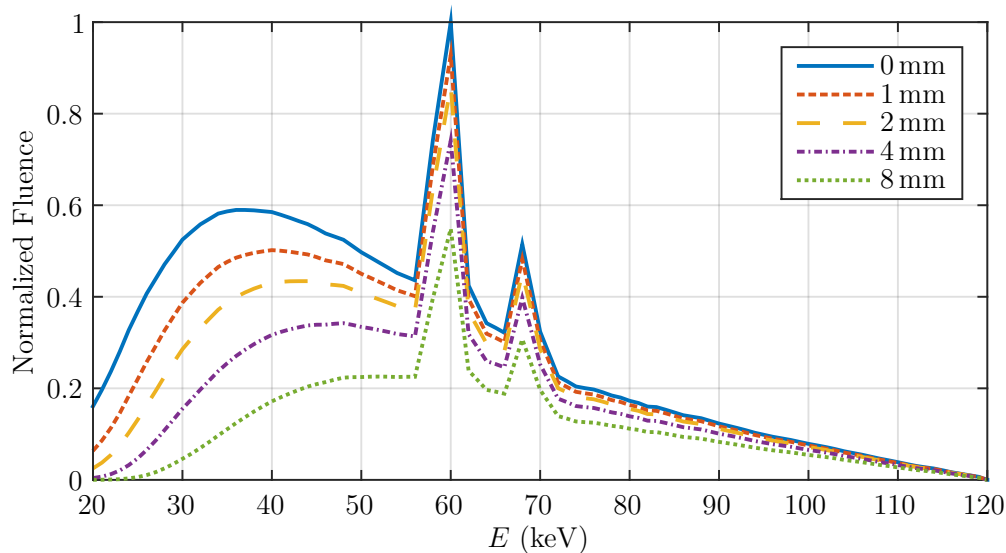
Figure 2.6: Examples of effect of source filtration on an x-ray spectrum of a tungsten-anode tube. Filtration ranges from 0 mm to 8 mm of aluminum. Note the significantly larger effect on the lower end of the spectra than on the high end.

silicon technology, which is compatible with large area devices and hence allows for detector scaling in a cost-effective manner. Pixel electronic components and their necessary connections are fabricated through lithographic etching techniques. These components include both the driving electronics and a light-sensitive region that takes up most of the pixel area[9].

2.2.1 Indirect Detection

While FPDs are very sensitive to visible light, their component materials and their dimensions limit their capabilities of x-ray absorption to a small number of photons. To solve this issue, the concept of *indirect x-ray detection* is introduced. This technique consists of the addition of a scintillator layer that sits immediately on top of and is optically coupled to the TFT array. This new layer will absorb x-ray photons and convert them into optical light, which can then be more efficiently captured by the TFT array.

When an x-ray photon is absorbed at the scintillator, several optical photons are generated at the place where this interaction occurred. The number of said photons depends on the energy of the original incoming x-ray photon, E, and will be given by the *scintillator gain function*, $\tilde{Q}_{CsI}(E)$. Note that this function is actually a random function, since both x-ray absorption and light generation are statistical processes. Unfortunately, this function does not follow any typical distribution type, and thus cannot be easily described mathematically and must be empirically determined. It is, however, possible to calculate the *mean* of this function at any energy as

$$\bar{Q}_{CsI}(E) = \gamma(E)E_{abs}(E) \tag{2.3}$$

where $\gamma(E)$ (photons/keV) is the mean number of photons generated and collected in the scintillator due to an absorbed photon of energy E, and $E_{abs}(E)$ is the energy absorbed in the scintillator due to an x-ray photon of energy E interacting in it. For common inorganic scintillators, this gain is nearly proportional to the deposited radiation[6], which removes the energy dependence in the number of photons generated ($\gamma(E) = \gamma$) and reduces Equation (2.3) to $\bar{Q}_{CsI}(E) = \gamma E_{abs}(E)$.
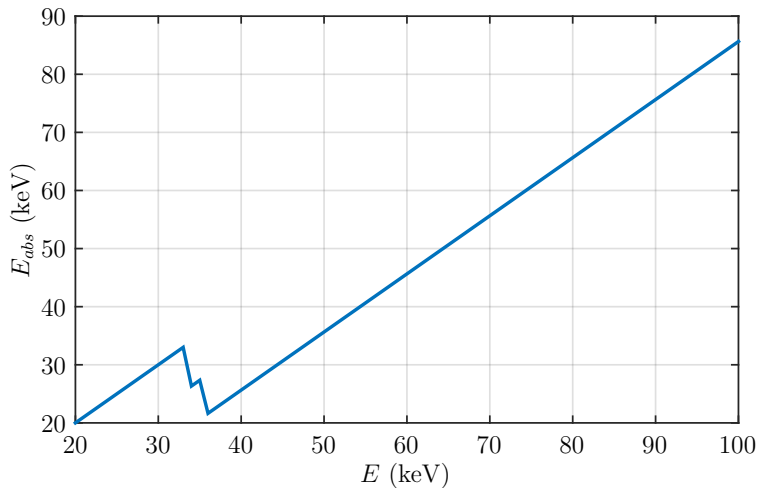
Figure 2.7: Energy absorbed into a Cesium Iodide scintillator as a function of incoming x-ray energy E. Note the dips at the material's transition energies of 33.2 keV and 36.0 keV. Data from [10].

A naive instinct might be that E_{abs} will simply be equal to E, since when a photon is absorbed in the scintillator, its energy must be conserved by the generation of new optical photons. However, when the energy of the x-ray photons incident on the scintillator exceeds a transition energy of the absorber, some of their energy will be lost in escaping characteristic x-ray emission[11]. Thus, E_{abs} cannot be so simple as it must take this effect into account. In fact, it has previously been calculated for certain scintillating materials[10] to be linearly dependent on E both below and above the K-edge energies, while showing considerable dips at those energies. Figure 2.7 shows an example of this for the common scintillator material of Cesium Iodide (CsI), where these dips are easily appreciable.

2.2.2 Blurring and Structured Scintillators

When an x-ray interacts in a scintillator, each light photon that is produced will propagate in any direction in the screen. Due to the amorphous structure of typical scintillators, these photons will refract off any number of small surfaces until they eventually either exit the scintillator, are reabsorbed into it, or are absorbed in the TFT array. Due to the isotropic nature of this transport, those photons that do reach the array will have spread about the interaction point. It is clear that this spread will result in a blurring of the original 2D signal carried in the x-ray beam[12]. This is easiest to understand through the example illustrated in Figure 2.8a, where an incoming infinitely thin pencil beam will spread to become a blurred dot that will resemble a Gaussian kernel.

A major conflict is caused by this blurring when attempting to increase the detection efficiency of a scintillator screen by increasing its thickness, since doing so will increase the optical photon spread and therefore the blurring. To alleviate this issue and obtain higher image resolutions, structured scintillators can be used in place of amorphous ones. When evaporating CsI in conjunction with Thallium (Tl) under the right conditions, a CsI:Tl mixture will condense in the form of closely packed micro-columnar structures[13, 14]. Due to the difference in refractive index between these CsI:Tl columns ($n = 1.79$) and the air surrounding them ($n = 1$), they can effectively act as microscopic optical fibres that guide the generated light photons in the vertical direction. The resulting reduction in signal spread can be seen illustrated in Figure 2.8b.

However, since the emission of optical photons is isotropic and total internal reflection will not be achieved for all angles in the columns, some of the light will still be scattered
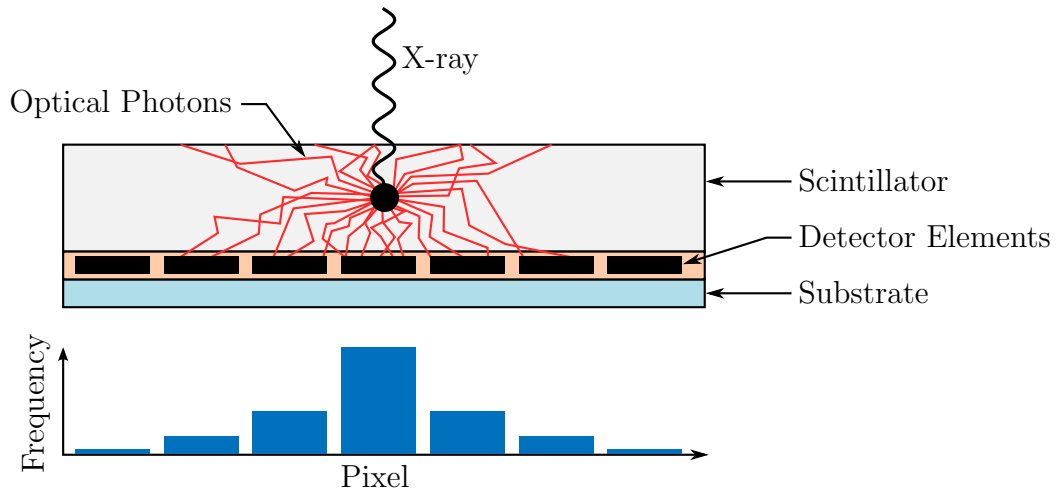
(a) Illustration of how the isotropic nature of the optical photon generation will result in a blurring effect. The photons produced due to the absorption of a single x-ray will refract through the scintillator due to its amorphous structure and either be absorbed at a pixel element or exit the absorber. The frequency of photons reaching each detector pixel is shown in the histogram, which clearly shows the lateral spread of a single-point signal.
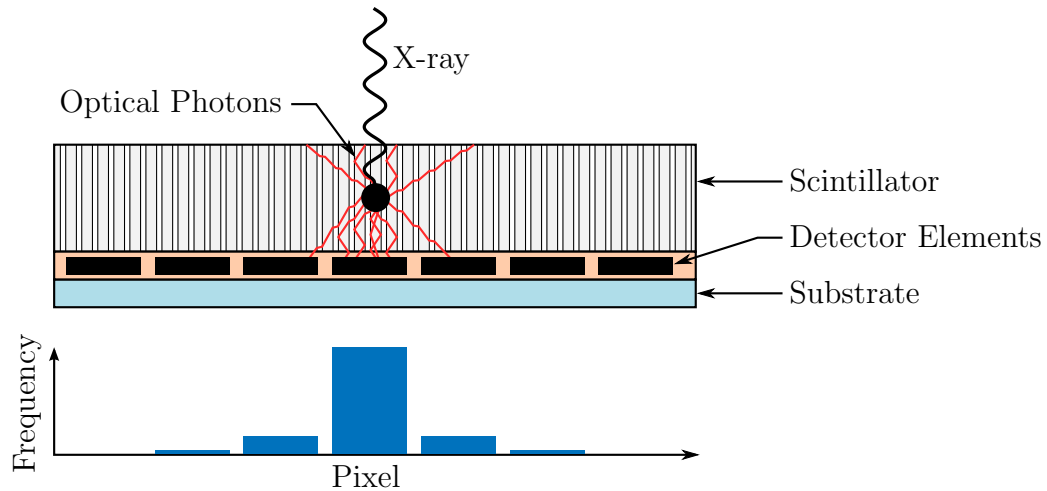
(b) Illustration of the increase in spatial resolution obtained by structured scintillators. The generated optical photons are guided through the columnar structure to either end of the scintillator, reducing lateral spread. The frequency of photons reaching the centre pixel will be significantly increased. Note that the scintillator structure is not to scale.

Figure 2.8: Comparison of optical mechanisms in amorphous and structured scintillators and their resulting signal spreads.

between pillars and travel laterally. In fact, theoretical calculation suggest that 17% of the light quanta generated will contribute to signal spread[15]. Moreover, these light-collimating capabilities will be reduced further by the inevitable nonuniformities formed in the scintillator during fabrication. Nonetheless, the addition of this structure in scintillators has been shown to allow for higher spatial resolution and even higher detection efficiency since CsI:Tl has a higher value of γ than conventional CsI.

2.2.3 The Point Response Function

The blurring caused by the scintillator and other factors can be hard to measure quantitatively. To solve this, we can introduce the Point Response Function (PRF), perhaps the most fundamental measure of imaging resolution properties. By definition, the PRF is the response of an imaging system to a point source. In other words, it is the image created in the detector by an incoming infinitely-thin x-ray pencil beam[3].

The PRF is typically described as a function of spatial dimensions as $\mathrm{PRF}(x, y)$. It is important to note that while it can sometimes be thought of as rotationally symmetric, a practical imaging system will have non-uniformities that will result not only in PRF asymmetries, but in a different PRF at different spatial portions of the detector.

(a) Input Pencil Beam **(b)** $\mathrm{PRF}(x, y)$
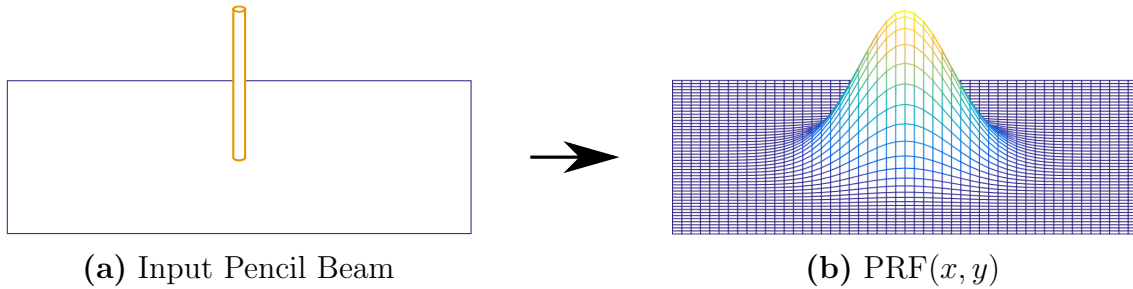
Figure 2.9: **(a)** A point source generates an x-ray pencil beam as the input to the imaging system that results in **(b)** the Point Response Function as the output, due to spatial spreading in the scintillator and other factors.

It is clear how the PRF can be used to describe the blurring introduced by a detector system on what is being imaged[16], since the acquisition of the PRF will emulate in a controlled manner the physical and processing events that take place when obtaining a regular image. An output blurred image of a detector system can now be thought of as the

convolution between an input unblurred image and the system's PRF. In other words, the PRF is considered to be the kernel that introduces blur by filtering an input image with it.

2.3 Relevant Statistics

Almost all physical elements in radiography are governed by stochastic processes. From the number and energy of x-ray quanta generated at the tube, to the absorption and scattering in the patient; from the photon detection at the sensor, to the noise associated with reading the image[17]. For this reason, it is important to understand the statistics these processes will follow. This section aims to summarize the theory behind the statistics relevant to this thesis' work.

2.3.1 Normal Distribution

The normal—or Gaussian—distribution is the most widely used in statistics. It describes a scenario in which the frequency of each observation will follow the well-known bell shape. Two parameters are needed to characterize a normal distribution: the mean, $\bar{x}$, and the standard deviation, σ. The *variance* of the distribution is defined as the square of the standard deviation, σ^2, but is not a third independent parameter. If a variable $\tilde{x}$ is governed by a normal distribution, the probability of it having a specific value x will be given by

$$P(x) = \frac{1}{\sqrt{2\pi}\sigma} e^{\left(\frac{x-\bar{x}}{\sqrt{2}\sigma}\right)}. \tag{2.4}$$

The most likely value of $\tilde{x}$ will therefore be $\bar{x}$, with this likelihood diminishing evenly for higher and lower values at a rate determined by σ. The independence of the two distribution parameters makes the normal distribution very flexible and able to describe many physical phenomena. This flexibility is clear in Figure 2.10, where the effects of each parameter on the distribution shape are exemplified.
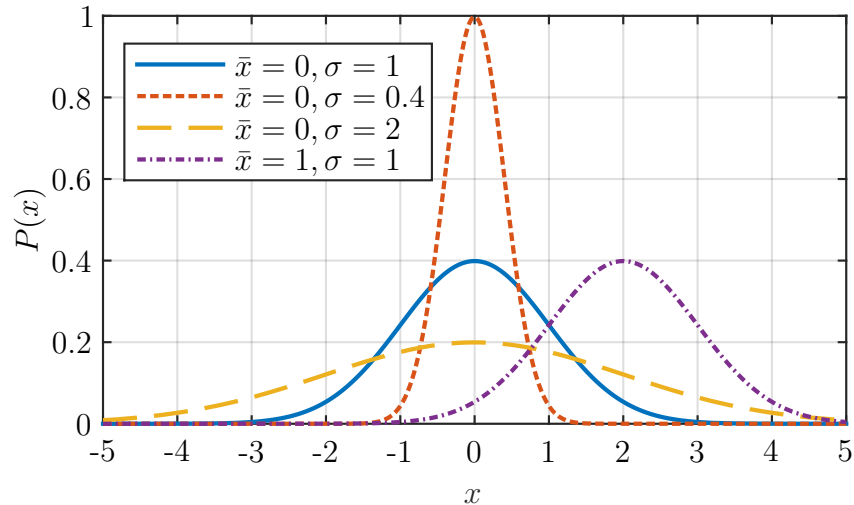
Figure 2.10: Selection of probability density functions of the normal distribution. The mean $\bar{x}$ and standard deviation σ are varied in each example given to illustrate the flexibility of this distribution.

2.3.2 Poisson Distribution

A distribution that is particularly relevant to radiological imaging is the Poisson distribution. It is used to express the probability of independent events occurring in a fixed interval of time or space. Interestingly, the entire shape of this distribution is only governed by one parameter: the mean, $\bar{x}$. This is evident in its mathematical definition which for a random variable $\tilde{x}$ equaling a value x would be

$$P(x) = \frac{\bar{x}^x}{x!}e^{-\bar{x}}. \tag{2.5}$$

An interesting property of the Poisson distribution is that for sufficiently large values of $\bar{x}$, it can be approximated extremely well with a normal distribution of mean $\bar{x}$ and standard deviation $\sigma = \sqrt{\bar{x}}$. Figure 2.11 shows the close resemblance of these two distributions, which will only become closer for larger values of $\bar{x}$. This will become very important for the work in this thesis, as simply knowing the mean value of a particular phenomenon that is known to follow a Poisson distribution is enough to approximate it using a normal distribution and hence learn its standard deviation and variance if this value is large enough.
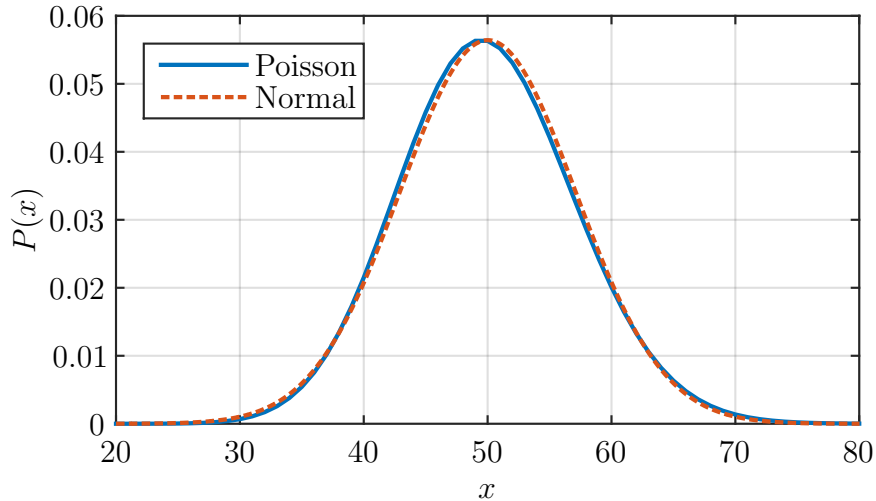
Figure 2.11: Comparison of a Poisson distribution of mean $\bar{x} = 50$ with a normal distribution of mean $\bar{x} = 50$ and standard deviation $\sigma = \sqrt{\bar{x}} = \sqrt{50}$ to show the quality of the approximation. As $\bar{x}$ increases further, the two functions resemble each other even closer.

2.3.3 X-ray Emission and Absorption

Much like other particle emission—like, for example, gamma rays due to atomic decay—the production of x-rays in a tube is known to follow a Poisson distribution. Therefore, the mean number of generated photons in the source will see a Poisson-like spatial variation, and the number of photons that reach each unit area in the detector will be governed by this distribution.

Also importantly, since the probability that an emitted x-ray photon (that has not interacted with the object being imaged) will be absorbed in a particular detector pixel is small and constant, the fluctuations in absorbed quanta between one pixel to the next will follow the Binomial law[17, 11]. Mathematically, if a single photon has a chance ρ of being absorbed in the detector sensitive material, the probability that n out the m x-rays that reach the detector pixel will be absorbed in it is given by $P(n|m) = \frac{m!}{n!(m-n)!}\rho^n (1 - \rho)^{m-n}$.

Interestingly, when considering the number of photons that will be counted at each pixel, these two phenomena are combined and the resulting distribution is also Poisson[18]. This is quite fortunate for radiography, as the mean number of x-rays recorded in each detector element, $\bar{N}$, will be large enough that a normal function can be used to closely approximate

17

its distribution. In turn, the variance between pixels can be very easily calculated as

$$\sigma^2 = \bar{N}. \tag{2.6}$$

Since pixel value variance is the measure normally used to represent image noise, Equation (2.6) can be used to easily calculate the contributions that the Poisson spatial variance of the number of x-rays in the beam and the binomial distribution of absorbed photons in each pixel have on the final image noise. This measure is know as the quantum noise of the image, and it is possible to calculate its theoretical value simply by knowing $\bar{N}$.

2.3.4 Random Variable Operations

When dealing with random variables—that is, variables that follow a random function—it is often useful to analyze how certain operations will affect their distribution. Of particular interest to the work presented in this thesis are the changes when scaling a random variable by a constant, the distribution propagation when summing several random variables, and the effects on a random variable's mean and variance when applying a function to it.

The first relevant property involves a random variable $\tilde{x}$ with mean $\bar{x}$ and variance $Var\{\tilde{x}\} = \sigma^2$ that is multiplied by a constant C. Its new mean and variance are often of interest and can be easily calculated using

$$\overline{C\tilde{x}} = C\bar{x}, \tag{2.7}$$

$$Var\{C\tilde{x}\} = C^2 Var\{\tilde{x}\} = C^2\sigma^2. \tag{2.8}$$

These simple fundamental properties of the mean and variance apply to any random variable, regardless of the distribution they follow, and they will prove extremely helpful when developing the analytical model presented here.

The next interesting property refers to a variable that is defined as the sum of several independent random variables. If $\tilde{Y}$ is defined as the sum of n random variables $\tilde{x}_i$ as $\tilde{Y} = \sum_{i=1}^{n} \tilde{x}_i$, then its mean and variance are a simple function of the means and variances of the individual x_i variables as[19]

$$\bar{Y} = \sum_{i=1}^{n} \bar{x}_i, \tag{2.9}$$

18

$$Var\{\tilde{Y}\} = \sum_{i=1}^{n} Var\{\tilde{x}_i\}. \qquad (2.10)$$

Lastly, it is relevant to analyze the results of applying arbitrary functions to single random variables. While mathematical analysis of functions of random variables provide solutions only for simple cases (e.g. the linear product detailed above), exact solutions cannot be found for more complex function. However, it is possible to find close approximations through the Taylor Series method[19]. The conclusion of this method states that for a function of a random variable $g(\tilde{x})$, the resulting mean and variance can be approximated to a first-order as

$$\overline{g(\tilde{x})} \approx g(\bar{x}) \qquad (2.11)$$

$$Var\{g(\tilde{x})\} \approx \left(\frac{dg(x)}{dx} \Big|_{x=\bar{x}} \right)^2 Var\{\tilde{x}\}. \qquad (2.12)$$

2.4 Dual-Energy Imaging

The quality of a medical image and by extension its value as a tool depends only on how well it can convey the anatomy of the patient being imaged to the observer. The better the anatomy is understood, the more accurate information a physician has to make decisions. A large source of noise that often decreases the quality of an image is anatomical noise. It is caused by a superposition of the normal anatomy that stems from the 2D projection of the 3D patient. This noise can obscure the tissue being imaged or can be misread as anatomical abnormalities. A simple example of this is a chest radiograph that is acquired with the intention of evaluating pulmonary anatomy, which is inevitably obstructed by the ribs in the obtained image. In this case, the ribs are a major source of anatomical noise, as they are not the anatomy of interest.

A powerful technique that was proposed as far back as 1976 by R. Alvarez and A. Macovski[20] to reduce anatomical noise is Dual-Energy (DE) Imaging. This technique exploits a fundamental property of x-ray and matter interaction: not only will different tissue types have different mass attenuation coefficients ($\mu/\rho(E)$) across the diagnostic energy range, but the rate of change of these coefficients will also differ. This effect can be seen in Figure 2.12 when comparing the coefficient values at the low end of the spectrum ($\sim 40\,\text{keV}$) with the high end ($\sim 100\,\text{keV}$). It is clear that the difference between the

coefficient values of each tissue type will change as one moves across the spectrum. For instance, the difference in μ/ρ between bone and soft tissue is $\sim 0.397\,\mathrm{cm}^2/\mathrm{g}$ in the low end, while it is only $\sim 0.016\,\mathrm{cm}^2/\mathrm{g}$ at the high end.
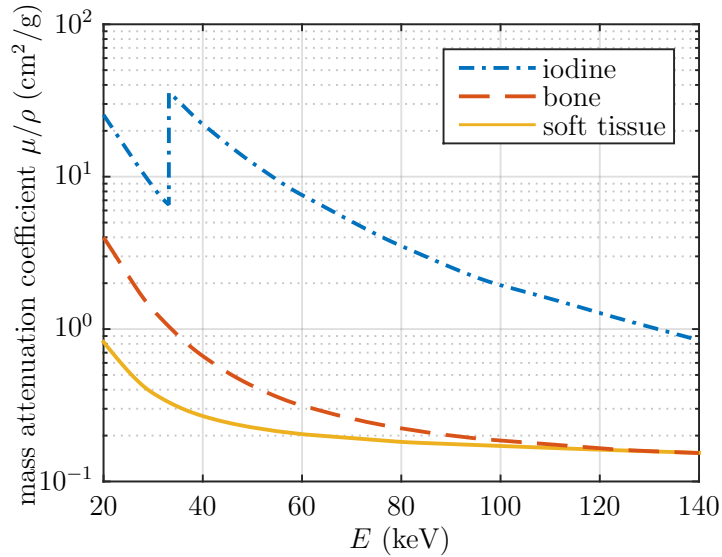
Figure 2.12: Mass attenuation coefficients over the diagnostic x-ray energy range for iodine, cortical bone and soft tissue. The rate of change across this range for each material's coefficient is noticeably distinct among the different materials. Data from [21].

DE imaging takes advantage of this property and intelligently combines two images—one obtained with low-energy (LE) and one with high-energy (HE) photons[22]—to generate one or two enhanced images. Each of these enhancements aims to remove anatomical noise by isolating the patient's highly-attenuating tissue components from its soft-tissue (or low-attenuating) components. Depending on what type of tissue is of interest to a radiologist, any of the two images can be used to observe a particular part of the anatomy without noise contributions from the other[23, 24]. For example, two images are typically obtained in DE chest radiography, one containing soft-tissue only and one bone only. This provides an enormous advantage over single-energy imaging, as images with much better information content and without clutter from other tissue types can be produced.

2.4.1 Obtaining the LE and HE Images

The greatest challenge in DE imaging comes from the need to obtain the two separate low- and high-energy images. To achieve this, the x-ray spectrum that is absorbed at the detector should be heavily weighted in the low end of the diagnostic range for the LE image, and in the high-end for the HE image. Obtaining this spectral separation can be done in two fundamentally different ways: either the source spectrum differs for the two images, or the detector selectively absorbs different parts of a wider spectrum to form each image. This section will detail the current practical implementations of these two approaches. Regardless of the method, a large separation of the two spectra is imperative in obtaining the final images, since a difference in the rate of change of μ/ρ is needed.

kVp Switching

Perhaps the most straightforward way to take two images at different energies is to obtain one immediately after the other changing no part of the imaging system but the spectrum the x-ray tube generates. This is the concept behind kVp switching (sometimes called double-shot radiography), where a first image is taken using a low x-ray tube kVp and, immediately after, a second image is obtained with a high kVp[25]. Since the low- and high-kVp beams will have different effective energies, the two resulting images will contain mainly information obtained in the low and high ends of the x-ray diagnostic spectrum, respectively.

kVp switching results in excellent spectral separation between the two images and minimizes the overlap between the images' spectra. However, the temporal separation that is inherent of this technique will cause motion artifacts to appear in the final images, which can pose a large challenge to a radiologist interpreting it. These artifacts are noticeable distortions in the image caused by slight misalignments of the anatomies in the LE and the HE image. They stem from patient motion that occurs during and in between the images acquisitions.

Ideally, the source tube voltage could be changed instantaneously such that as soon as one exposure is finished, the next one can begin. However, current commercially-available sources require an interval between the successive exposures of at least 150 ms to 200 ms. This is due not only to a changing voltage but also because a change in tube current is also needed to achieve the ideal relative intensities of the two images. While this interval is short

enough for most patients to be able to refrain from large movements, cardiac, respiratory and small muscular motions are bound to occur throughout it. Motion artifacts will appear due to these movements, which can be a particular hindrance in cardiac and pulmonary imaging due to the large presence of the heart and the lungs.

It is possible to address the issue of motion artifacts by using a dual-source system where a different x-ray tube is used for each image and, when timed correctly, the interval between exposures can be minimized. While this is somewhat common practice for computed tomography setups[26], when applied to radiography, the slight difference in projection angle between the two images means that some post-processing is required, and thus some other artifacts could be introduced.

One of the largest drawback that kVp switching systems have in real-world applications is financial. These setups require an x-ray source capable of producing two very different spectra in a very short time, which is not compatible with typical chest radiography setups. A new source is thus required, which can be costly, a problem that is even larger for a dual-source system. Moreover, the two separate exposures mean a higher dose delivered to the patient when compared to conventional radiography, although this increase is fairly small at $\sim 15\,\%$[27].

Single-Shot Imaging

An alternative method for obtaining both images was proposed by Alvarez and Macovski in 1976[20] and applied to radiography by Barnes *et al* in 1985[28]. Commonly referred to as *single-shot* DE imaging, it takes the opposite approach than kVp switching and achieves spectral separation in the detector and not at the source. This is accomplished by stacking two sensor layers vertically to form a double-layer detector in what is known as a sandwich configuration[29, 30, 31, 32]. As shown by the normalized spectra in Figure 2.13, the top layer absorbs mainly LE x-rays while the bottom absorbs the HE x-rays. Only a single exposure is hence necessary with this technique, which is done at a higher kVp to allow for a large spectrum that covers both LE and HE x-rays.

The spectral separation between the top and bottom layers stems from a combination of two factors. First, since the attenuation coefficient is lower for HE x-rays, these have an intrinsically higher probability of going through the top layer unabsorbed. Hence, the bottom layer is reached by a lower number of photons but of a larger proportion of HE
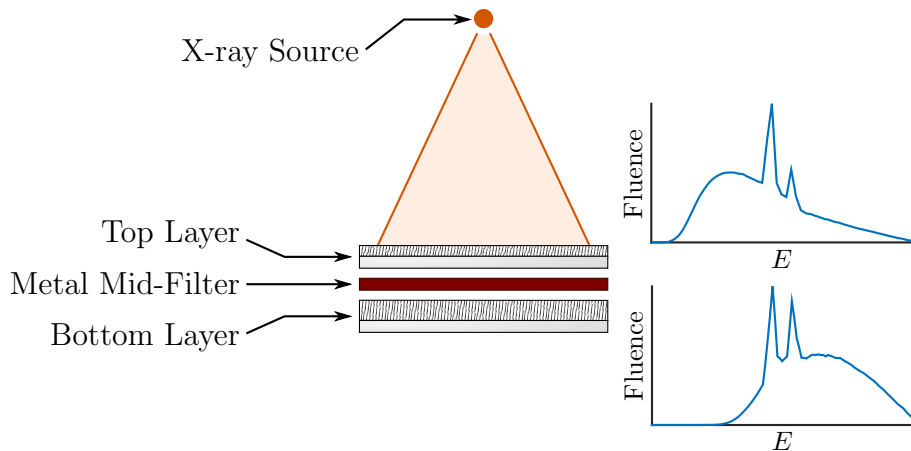
Figure 2.13: Diagram of a typical dual-layer detector used in single-shot DE imaging. The detector consists of two stacked sensitive layers and a metal mid-filer in between them. Typical normalized fluences at the top and bottom sensor are shown, and illustrate the spectral separation between the layers.

Bremsstrahlung x-rays than LE ones, allowing this layer to form the HE image. Second, a metal mid-filter is placed in between the top and bottom sensitive layers (hence the name of sandwich configuration) that will harden the beam further before it reaches the bottom layer. Much like the source filtration discussed in Section 2.1.3, the presence of this filter allows a higher number of HE photons than LE photons through, further contributing to the spectral separation.

The single exposure needed in this technique results in two clear advantages of single-shot imaging. First, the total dose delivered to the patient will naturally be lower when compared to the two exposures of kVp switching[25]. Second, since the two images are obtained simultaneously, single-shot imaging is considered immune to the motion artifacts that affect kVp switching. As mentioned previously, this presents a large advantage when dealing with cardiac and pulmonary images, especially.

Unfortunately, due to the lower number of x-ray photons reaching the bottom sensor, the HE image will be noisier than the LE image, or even than a normal radiograph. While this can be compensated in post-processing, the resulting DE images will be noisier in single-shot than for kVp switching. Furthermore, the method of spectral separation used by this technique has also been shown to be less effective than kVp switching[32, 33]. In

turn, this results in further noise of the final DE images and a lower suppression of the desired anatomical noise.

Single-Shot	kVp Switching
• Normal dose delivered to patient	• Increased dose delivered to patient
• Limited energy separation	• Better spectral separation
• Noisier image due to photon loss	• Lower image noise
• Immune to motion artifacts	• Susceptible to motion artifacts
• Requires a specialized detector	• Can use conventional detectors
• Can use current x-ray sources	• Needs a fast-switching source

Table 2.1: Advantages and disadvantages of either mature method to obtain the high- and low-energy images required for Dual-Energy images.

2.4.2 Combining the Images

The advantage of DE imaging over conventional radiography comes from its ability to decompose the patient's projection into soft-tissue- and hard-tissue-only images. Several mathematical methods exist for obtaining these DE images from the LE and HE inputs[34], most notably *logarithmic subtraction* and *basis decomposition*[35]. This thesis will focus on the former, since it is not only one of the simplest, but has also proven to be quite effective at obtaining the desired result[23].

We can begin to understand the way in which logarithmic subtraction can be used to obtain the enhanced DE images by considering the Beer-Lambert law (Equation (2.1)) for an object that contains both soft and hard tissue:

$$I(E) = I_0(E)e^{-(\mu_s(E)t_s + \mu_h(E)t_h)} \tag{2.13}$$

where $I_o(E)$ is the fluence of the incident x-ray beam, $\mu_s(E)$ and $\mu_h(E)$ are the attenuation coefficients of the soft and hard tissue respectively, E is the x-ray energy, t_s and t_h are the thicknesses of each material, and $I(E)$ is the resulting transmitted x-ray fluence.

24

In a DE imaging system, two separate incoming x-ray fluences must be considered: that of the input beam used for generating the LE ($I_0^L(E)$) and that for the HE ($I_0^H(E)$) image. We consider the idealized scenario in which these are monoenergetic beams of a single low (E_L) and high (E_H) energy, and hence $I_0^L(E) = I_0^L \delta(E_L)$ and $I_0^H(E) = I_0^H \delta(E_H)$. The monoenergetic x-ray intensities reaching the detector for each of the images can then be expressed as

$$I^H = I_0^H e^{-(\mu_s(E_H)t_s + \mu_h(E_H)t_h)} \tag{2.14}$$

$$I^L = I_0^L e^{-(\mu_s(E_L)t_s + \mu_h(E_L)t_h)} \tag{2.15}$$

where I^H and I^L will form the high- and low-energy images, respectively.

Logarithmic subtraction defines a new enhanced hard-tissue image by subtracting the natural logarithm of a weighted LE image from the HE one, or[36, 22]

$$I_{DE}^h \equiv \ln\left(I^H\right) - w_h \ln\left(I^L\right) \tag{2.16}$$

where I_{DE}^h is the enhanced DE image that will contain anatomical information only from the hard-tissue components, and w_h is a weighting factor. This definition can be expanded using Equations (2.14) and (2.15) into

$$
\begin{aligned}
I_{DE}^h &= \ln\left(I_0^H e^{-(\mu_s(E_H)t_s + \mu_h(E_H)t_h)}\right) - w_h \ln\left(I_0^L e^{-(\mu_s(E_L)t_s + \mu_h(E_L)t_h)}\right) \\
&= \ln\left(I_0^H\right) + \ln\left(e^{-(\mu_s(E_H)t_s + \mu_h(E_H)t_h)}\right) \\
&\quad - w_h \ln\left(I_0^L\right) - w_h \ln\left(e^{-(\mu_s(E_L)t_s + \mu_h(E_L)t_h)}\right) \\
&= k_h - (\mu_s(E_H)t_s + \mu_h(E_H)t_h) + w_h\left(\mu_s(E_L)t_s + \mu_h(E_L)t_h\right)
\end{aligned}
\tag{2.17}
$$

where k_h is defined as $k_h \equiv \ln\left(I_0^H\right) - w_h \ln\left(I_0^L\right)$ and can be considered a constant offset on the image since it is independent of the thicknesses and attenuation coefficients of the soft- and hard-tissue materials.

By intelligently defining w_h such that the soft-tissue contrast can be removed, the final desired enhanced DE hard-tissue-only image can be obtained from I_{DE}^h. Close examination of Equation (2.17) will reveal that the ideal value for w_h to achieve this is

$$w_h = \frac{\mu_s(E_H)}{\mu_s(E_L)}. \tag{2.18}$$

25

The enhanced DE image then becomes

$$
\begin{aligned}
I_{DE}^h &= k_h - (\mu_s(E_H)t_s + \mu_h(E_H)t_h) + \frac{\mu_s(E_H)}{\mu_s(E_L)}\left(\mu_s(E_L)t_s + \mu_h(E_L)t_h\right) \\
&= k_h - \mu_s(E_H)t_s - \mu_h(E_H)t_h + \mu_s(E_H)t_s + \frac{\mu_s(E_H)\mu_h(E_L)}{\mu_s(E_L)}t_h \\
&= k_h - \mu_h(E_H)t_h + \frac{\mu_s(E_H)\mu_h(E_L)}{\mu_s(E_L)}t_h \\
&= k_h + t_h\left(w_h\mu_h(E_L) - \mu_h(E_H)\right)
\end{aligned}
\tag{2.19}
$$

which is completely independent of the thickness of soft tissue t_s. The resulting image will hence contain hard-tissue information *only* and have its soft-tissue anatomical noise removed. Even in more realistic scenarios where multiple types of tissues are present, this technique will still cancel all soft-tissue contrast in the enhanced image and remove its anatomical noise. It is hard to overstate the utility of such a simple technique to mathematically isolate a particular type of tissue (and a particular type of anatomy) from a radiographic image. The image enhancements have been shown to allow for better diagnoses that are not clouded by anatomical noise.

The same procedure can be repeated to obtain an enhanced image I_{DE}^s that contains only information from the soft-tissue components. Similarly to before, it is defined as

$$
I_{DE}^s \equiv \ln\left(I^H\right) - w_s \ln\left(I^L\right)
\tag{2.20}
$$

where the weighting factor is in this case tuned to negate hard-tissue terms as

$$
w_s = \frac{\mu_h(E_H)}{\mu_h(E_L)}.
\tag{2.21}
$$

Equation (2.20) can now be expanded similarly to before using the constant $k_s \equiv \ln\left(I_0^H\right) - w_s \ln\left(I_0^L\right)$ to obtain a hard-tissue-independent result

$$
\begin{aligned}
I_{DE}^s &= \ln\left(I_0^H e^{-(\mu_s(E_H)t_s + \mu_h(E_H)t_h)}\right) - w_s \ln\left(I_0^L e^{-(\mu_s(E_L)t_s + \mu_h(E_L)t_h)}\right) \\
&= \ln\left(I_0^H\right) - (\mu_s(E_H)t_s + \mu_h(E_H)t_h) \\
&\quad - w_s \ln\left(I_0^L\right) + w_s\left(\mu_s(E_L)t_s + \mu_h(E_L)t_h\right) \\
&= k_s - \mu_s(E_H)t_s - \mu_h(E_H)t_h + \frac{\mu_h(E_H)\mu_s(E_L)}{\mu_h(E_L)}t_s + \mu_h(E_H)t_h \\
&= k_s + t_s\left(w_s\mu_s(E_L) - \mu_s(E_H)\right),
\end{aligned}
\tag{2.22}
$$

allowing for the enhancement of soft tissue in the image and the removal of anatomical noise caused by hard tissue.

In practice, a total cancellation of a specific tissue type is not commonly possible. Several factors will contribute to form a non-ideal scenario that cannot be captured by the equations above. Some of the largest of these are: the broad spectrum of the x-ray fluences that will lead to the formation of each image as opposed to the idealized monoenergetic sources used in the mathematical analysis; inhomogeneities in the density or mass attenuation coefficient of the tissue being canceled which make it impossible to determine the exact value that should be used when calculating the weighting factor; and x-ray scatter from both the object being imaged and the detector that are not accounted by Beer-Lambert law. These nonidealities also mean that the theoretical value of w_h and w_s from Equations (2.18) and (2.21) may not provide the best possible cancellation. Their ideal value is often calculated experimentally or qualitatively by the observer.

Note that while some applications often benefit from obtaining both types of enhanced images, the work presented in this thesis will focus on hard-tissue-only images because of the target applications chosen.

Chapter 3

Proposed Detector

3.1 Target Applications

Several radiography diagnostic and screening techniques depend on the visualization of small objects with a high attenuation coefficient embedded in an inhomogeneous soft-tissue environment. Dual-Energy imaging is a perfect tool for these types of techniques since it excels at eliminating the contrast of soft-tissue backgrounds and enhancing the detectability of such small objects. Two particular examples of these techniques will be investigated in this thesis as canonical representations of applications where the technology proposed here can improve on the state-of-the-art.

The first application studied is coronary angiography[37, 38]. In it, the arteries in and around the heart are imaged thanks to the injection of a safe contrast agent. Common purposes for this type of imaging are cardiovascular procedures—the most notable of which is cardiac catheterization—and the assessment of cardiovascular diseases. The contrast agent used contains a high amount of the heavy element iodine, which has a high attenuation coefficient (see Figure 2.12). The applications of DE imaging here are clear; the vessels containing this high-Z material are located in an environment of cluttered soft tissue (heart, lungs, etc.), so removing this background anatomical noise can improve their visualization[24].

The second imaging technique explored is calcification detection in chest radiography[39, 40, 41]. When a single pulmonary nodule is found on a conventional radiograph of the

chest, the only immediate way of testing its benignity or malignity is to analyze the presence and/or pattern of a calcification within it. Detection of these calcifications can be very difficult with conventional radiography due to their small size and anatomically noisy environment. DE imaging has been shown to aid in their detection and characterization[42] thanks to its ability to produce material-specific images, where a hard-tissue image can more clearly depict a nodule calcification.

3.2   Detector Design

The advantage of single-shot DE imagers over the kVp switching systems detailed in Section 2.4.1 of being immune to image artifacts caused by patient motion is very attractive for the two applications of interest mentioned above. The proximity to the heart and lungs in both techniques means that involuntary motion is inevitable, and thus a DE system that is not affected by it will see a large increase in the detectability of the objects of interest (be it the iodinated vessels or pulmonary calcifications).

However, by nature of its design, single-shot systems require a beam-hardening mid-filter. This filter will absorb a portion of the x-rays that reach it, which are essentially wasted in it as a result. Due to the necessary dose that must be delivered to the patient in order to obtain this image, it is imperative to extract as much information as possible from the x-ray signal that reaches the detector. The presence of this filter and the x-rays wasted in it go against this practice and are considered to negatively affect patient dose efficiency.

To address this issue, I propose a new detector design to be used for the aforementioned applications. Its basic configuration is shown in Figure 3.1 and is comprised of three stacked x-ray sensors. Each of these constitutes an individual layer of this three-layer detector, and consists of an amorphous silicon (a-Si) flat-panel sensor coupled to a scintillator layer. The thickness of the scintillating material is specific to each layer and is denoted t_t, t_m and t_b for the top, middle and bottom layers, respectively. While a small air gap is to be expected in real-world devices, each layer would ideally be placed immediately on top of the next one.

Each individual sensing layer will obtain its own image which will be distinct from the other two by the x-ray spectrum that reaches it. The top layer is designed to have a thinner
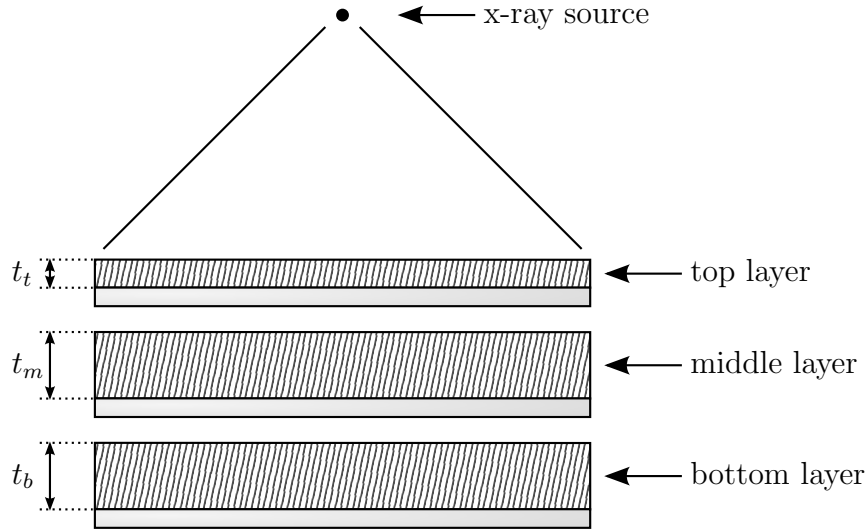
Figure 3.1: Diagram depicting the three-layer design of the proposed detector, where each layer is composed of a scintillating material of individual thickness coupled to an a-Si flat-panel sensor.

scintillator and will thus probabilistically absorb more of the lower end of the incident x-ray spectrum. The scintillator of the middle layer is made to be thicker and will absorb x-rays from across the entire spectrum, including most of the remaining LE photons. The bottom layer will therefore see mostly HE x-rays, and its scintillator is designed to be thick enough to absorb photons in this spectral range. This difference in incoming spectra is best illustrated in Figure 3.2, where the normalized fluence at each layer is shown for an example configuration of this three-layer detector.

3.2.1 Detector Operation

The ability to obtain all three images simultaneously during the same exposure allows this proposed detector to operate in a few distinct modes. Each mode involves a different way of combining the images from each detector layer with the purpose of obtaining one or more final enhanced images. Two main operational modes stand out and are the motivation behind this three-layer design.

The first mode is as a single-shot DE imager, in which only the signals from the top and bottom layers are used to create an enhanced DE image without the inhomogeneities

30
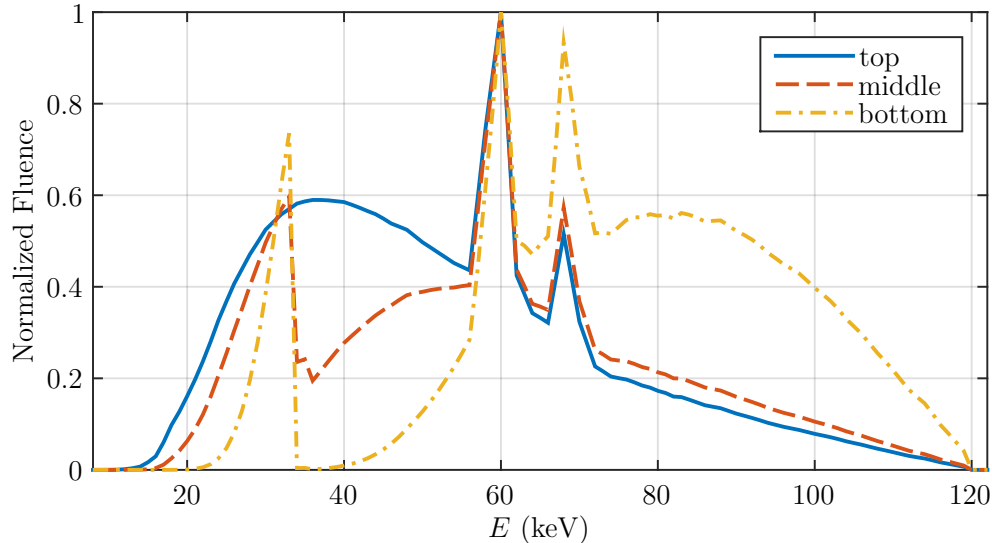
Figure 3.2: Normalized spectra incident on each of layer of a typical configuration of the proposed three-layer detector with CsI:Tl as its scintillating material.

of the soft-tissue components. Much like in the standard sandwich configuration, the top and bottom layers will form the low- and high-energy images respectively, but unlike said configuration, it is the middle sensitive layer that will act as a filter and harden the x-ray beam before it reaches the bottom layer. By independently tuning all three scintillator thicknesses, it should be possible to obtain sufficient spectral separation between the top and bottom layer to create the desired hard-tissue-enhanced images using logarithmic subtraction. Even though the scintillating material of the middle layer will have different attenuation characteristics than a conventional metal mid-filter, it may be possible to compensate for this by intelligently choosing its thickness to obtain the best possible spectral separation.

The second operational mode is as a conventional radiography (CR) detector, in which the signals from all three sensitive layers are simply added to form a single final image. In this mode, no dose delivered to the patient is wasted in a mid-filter and the image obtained will display information from the entire x-ray spectrum used. The ability to function in this mode sets this detector design apart from a conventional sandwich configuration, and provides an undeniable advantage over that entire class of detectors.

It is important to note that these two modes are not mutually exclusive, and that both resulting image types can be obtained simultaneously during a single exposure. If the DE-enhanced images rival those of a typical single-shot detector, this proposed design presents an alternative to the established technology with the important added benefit of being able to simultaneously obtain conventional radiographic images at no clear detriments. The only potential added downside of the three-layer configuration would be that of cost, but the recent decrease in price of flat-panel digital x-ray detectors is quickly removing this barrier, making this design more attractive.

Chapter 4

Analytical Model

This section will develop the mathematical and analytical model used to optimize the proposed detector and its imaging system. Several fabrication parameters will affect the performance of the device, and thus their individual effect on the quality of the resulting DE image is investigated. With this model, it is later possible to find the ideal combination of parameter values that will obtain the best possible enhanced images for each application.

4.1 Signal and Noise for Single-Layer Imagers

Each one of the layers in the proposed three-layer imager can be thought of as a single x-ray flat-panel detector. Therefore, the natural way to approach the development of an analytical model for the full detector is to begin by analyzing signal and noise of a conventional single-layer detector. This will then be expanded to all three layers and used to evaluate the performance of the proposed detector.

4.1.1 Signal Calculations

We begin by considering a single exposure of an x-ray spectrum $\Phi(E)$ (photon/(cm^2 keV)) through an object and to a scintillator-based FPD. Two possible x-ray paths stand out and must be considered to best evaluate performance. The first will only go through soft tissue of thickness t_s (cm) before reaching the detector, and will form what is considered

as the background of the image. The second will go through a highly-attenuating object of interest of thickness t_h (cm)—which in the considered applications is either an iodinated vessel or a calcified nodule—as well as its surrounding soft tissue before it reaches the detector. These two distinct paths are clearly illustrated in Figure 4.1 below.
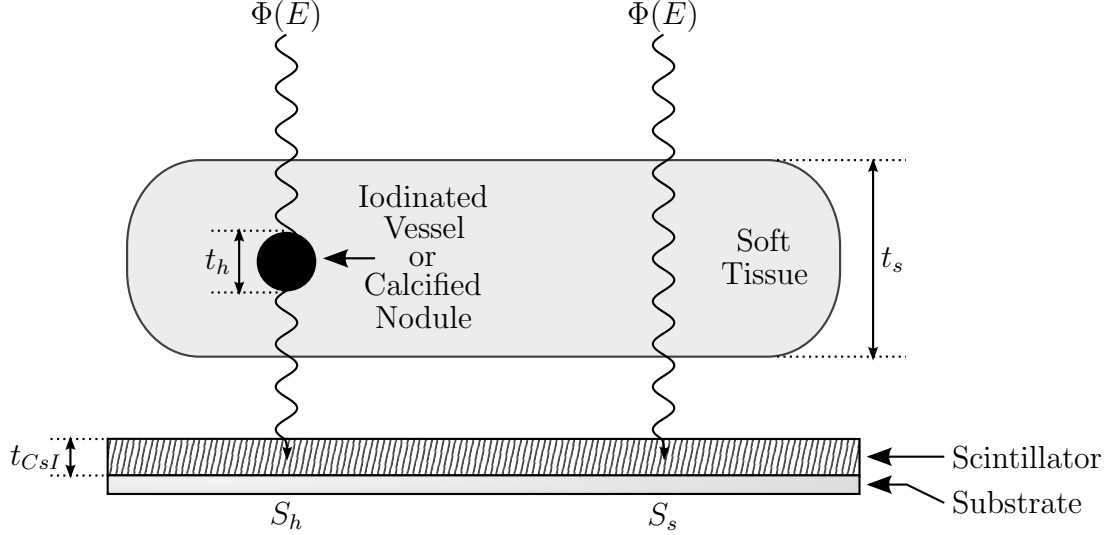
Figure 4.1: Diagram depicting the two possible x-ray paths of main interest for a single-layer conventional Flat-Panel scintillator-based detector.

The signals generated in the detector as a result of each of these paths are denoted S_s for the soft-tissue-only path and S_h for the path that includes an object of interest. These signals can also be thought of as the value of those detectors pixels located entirely inside the projection of one of these paths.

It is now possible to calculate the expected mean of these signals, $\bar{S}_s$ and $\bar{S}_h$, for a pixel of size A (cm^2) located in either path using[43]

$$\bar{S}_s = A \int_0^\infty \Phi(E) e^{-\mu_s(E)t_s} \eta(E) \bar{Q}_{CsI}(E) dE \tag{4.1}$$

$$\bar{S}_h = A \int_0^\infty \Phi(E) e^{-\mu_s(E)(t_s-t_h)-\mu_h(E)t_h} \eta(E) \bar{Q}_{CsI}(E) dE \tag{4.2}$$

where $\mu_s(E)$ and $\mu_h(E)$ are the x-ray attenuation coefficients (cm^{-1}) of soft tissue and the iodinated vessel or nodule calcification, respectively, at an x-ray photon energy E

(keV), $\eta(E)$ is the x-ray absorption ratio of the scintillator (i.e. its quantum efficiency), and $\bar{Q}_{CsI}(E)$ is the mean of the scintillator gain function (see Section 2.2.1). Note that I assume, for simplicity, that the attenuation coefficients are constant throughout each of the tissue types. In other words, both the object and the background are assumed to be uniform and lack inhomogeneities.

The quantum efficiency of the scintillator, $\eta(E)$, represents the fraction of x-rays absorbed by the scintillator (via any means of x-ray and matter interaction) out of those photons of energy E that have reached it. A value of 1 means that all x-rays of that energy would statistically be absorbed, while a value of 0 means no x-ray will interact with the scintillator. It is important to note that this represents the probability of an x-ray interacting with the scintillator, since x-ray and matter interaction is a stochastic process by nature. Its value at any arbitrary energy can be easily calculated using Beer-Lambert law (Equation (2.1)) as

$$\eta(E) = 1 - e^{-\mu_{CsI}(E)t_{CsI}} \tag{4.3}$$

where $\mu_{CsI}(E)$ is the attenuation coefficient of the scintillator (also considered constant across the entire scintillator) and t_{CsI} is the thickness of the scintillator.

The mean of the scintillator gain function can be calculated as described in Section 2.2.1 using

$$\bar{Q}_{CsI}(E) = \gamma E_{abs}(E). \tag{4.4}$$

Calculating this mean is of importance and will prove to be sufficient for building an analytical model. This will become evident when developing the following step of the model: the calculation of signal noise.

4.1.2 Noise Calculations

Since noise is an important measure that will affect the detectability of the objects of interest in our selected applications, being able to mathematically calculate it is imperative to building the analytical model. As mentioned in Section 2.3, image noise can be quantified by the variance of pixel values located fully in the same x-ray path. In other words, by the variances of $\tilde{S}_s$ and $\tilde{S}_h$; namely σ_s^2 and σ_h^2.

The largest contribution to the signal variance will be the number of photons of a particular energy that will be absorbed in the pixel, $\tilde{N}(E)$, which is known to follow a

Poisson distribution. If $\tilde{Q}_{CsI}(E)$ were constant for all energies, then the signals $\tilde{S}_s$ and $\tilde{S}_h$ would also follow a Poisson distribution and their variances would simply equal their mean values. However, the random nature of the scintillator gain function makes the obtained signals follow a product distribution[22]. Fortunately, since the number of scintillator photons generated for a typical x-ray is small when compared to N (e.g. a cesium iodide scintillator can generate $\sim$1500 optical photons for a 25 keV photon[8, 44, 45] while N is typically in the order of 20 000 for a typical radiograph of the chest[3]), its contribution to the signal variance can be neglected and only its mean value needs to be considered[11].

The linear variation in $\bar{Q}_{CsI}(E)$ values makes it necessary to sum the contributions of each spectral element individually when calculating the signal noise. Close inspection of Equations (4.1) and (4.2) reveals that they can be rewritten as simply $S = \int_0^\infty N(E)\bar{Q}_{CsI}(E)dE$, which, while useless for calculating actual values, can help simplify the noise derivation. At each component of the spectrum (or at each energy element of the integral) the contributions to the signal are $N(E)\bar{Q}_{CsI}(E)dE$, and, importantly, the scintillator gain can be treated as a constant. Therefore, the contributions to the variance of each component is simply a consequence of the product properties discussed in Section 2.3.4 and is expressed as $N(E)\bar{Q}_{CsI}^2(E)dE$[10]. To calculate the variance of the entire signal S, each contribution can be considered an independent random variable. Summing in quadrature through all these elements, the noise for the whole spectrum is hence

$$\sigma^2 = \int_0^\infty N(E)\bar{Q}_{CsI}^2(E)dE. \tag{4.5}$$

With this in mind, it is now possible to re-expand this expression for the expected variance in each one of the main-path signals as[11, 46]

$$\sigma_s'^2 = A \int_0^\infty \Phi(E)e^{-\mu_s(E)t_s}\eta(E)\bar{Q}_{CsI}^2(E)dE, \tag{4.6}$$

$$\sigma_h'^2 = A \int_0^\infty \Phi(E)e^{-\mu_s(E)(t_s-t_h)-\mu_h(E)t_h}\eta(E)\bar{Q}_{CsI}^2(E)dE. \tag{4.7}$$

Note that the notation for the equations above was slightly modified to represent the variance as σ'^2. The reason for this notation change is to emphasize that these variances include contributions only from the two random variables $\tilde{N}(E)$ and $\tilde{Q}_{CsI}(E)$. Further processes involved in image acquisition will affect the final signal variances. Most important

among these is the optical photon spread occurring in the scintillator. This effect still needs to be explored before the final signal variances of the analytical model can be obtained.

Scintillator Blur

While the needle-like arrangement of structured scintillators has been shown to guide light towards the top of and bottom surfaces of the screen and reduce lateral spread, a large number of light quanta are still likely to travel laterally before reaching the detector plane. This spatial spreading of the signal will inevitably reduce the maximum possible spatial resolution, but it will also have a smoothing effect that will reduce the spatial noise variance. It is imperative to calculate the expected signal spread and its effect on pixel value variance to fully develop an analytical model of noise.

Constructing a model to approximate the image blurring due to signal spreading in the scintillator begins by considering the Point Response Function of a structured scintillating screen of thickness t_{CsI}. Since the PRF is defined as the spread that occurs in a scintillator screen before the light quanta generated as a result of an infinitely thin monoenergetic x-ray pencil beam of energy E reach the detector plane, it will represent the deterministic scintillator blur[16]. The PRF will have a value at any point in the detector plane (x, y) and will be a function of the energy of the x-ray beam and the thickness of the scintillator. We can therefore write it as

$$\mathrm{PRF} = \mathrm{PRF}(x, y, E, t_{CsI}). \tag{4.8}$$

At this stage it is important to note that a simple mathematical calculation for the PRF is not possible due to the complexity of the scintillating material, its structure, and the ways in which it interacts with x-rays. Chapter 5 details the Monte Carlo simulations that were necessary to obtain PRF values when applying this model for detector-design optimization. For now, it is sufficient to consider the PRF as simply a known mathematical function that described scintillator blur.

Once the scintillator blur can be calculated, the next step is analyzing how it will affect the detector's signal variance. While the PRF is a continuous function, the image formed at the detector will be made up of individual pixels. Therefore, the blurring effect will be very dependent on the pixel pitch, p, of the detector. It is now necessary to consider a discrete function that describes the signal spread across the detector pixels. If

we consider the signal caused by an x-ray beam incident over an entire square pixel centred at $x = y = 0$, its spread to an arbitrary position in the scintillator (x, y) can be calculated by integrating PRF contributions from each area element in the pixel and will be expressed by the Interpixel Spread Function, or

$$\text{ISF}(x, y, E, t_{CsI}) = \int_{-\frac{p}{2}}^{\frac{p}{2}} \int_{-\frac{p}{2}}^{\frac{p}{2}} \text{PRF}(x - x', y - y', E, t_{CsI}) dx' dy'. \tag{4.9}$$

The ISF is still a continuous function through the detector, so it is now necessary to calculate how the signal incident over a pixel located at $i = j = 0$ will spread to its neighbouring pixels. In other words, how the continuous ISF function will be discretized into the detector pixels. The increase in signal that occurs in neighbouring pixels due to the spread of the x-rays incident across the entirety of the centre pixel is defined as $\Delta S_{i,j}$, where i and j represent the ith, j^{th} pixel of the detector array. This function of pixel position can be easily understood through the diagram in Figure 4.2, which clearly shows how the ISF is discretized into $\Delta S_{i,j}$. Mathematically, it is simply an integration of the ISF at the area occupied by the particular pixel, or

$$\Delta S_{i,j}(E, t_{CsI}) = \int_{p\left(j-\frac{1}{2}\right)}^{p\left(j+\frac{1}{2}\right)} \int_{p\left(i-\frac{1}{2}\right)}^{p\left(i+\frac{1}{2}\right)} \text{ISF}(x, y, E, t_{CsI}) dx dy. \tag{4.10}$$

Lastly, a normalized version of ΔS is defined as $\Delta S'$, and can be easily calculated using

$$\Delta S'_{i,j}(E, t_{CsI}) = \frac{\Delta S_{i,j}(E, t_{CsI})}{\sum\limits_{i=-\infty}^{\infty} \sum\limits_{j=-\infty}^{\infty} \Delta S_{i,j}(E, t_{CsI})}. \tag{4.11}$$

This normalized function is of importance because it can be thought of as the smoothing kernel that is applied to an unblurred image as a result of the signal spread, assuming that we are operating in a large-pixel regime where it will be fairly uniform and continuous. Using this analogy to simple image processing filtering, an image that was calculated assuming an ideal non-blurring scintillator can be transformed into a blurred version simply by convolving it with $\Delta S'$. For simplicity, I fit $\Delta S'$ to a two-dimensional discrete Gaussian kernel of standard deviation σ_G since we know that its convolution with a zero-
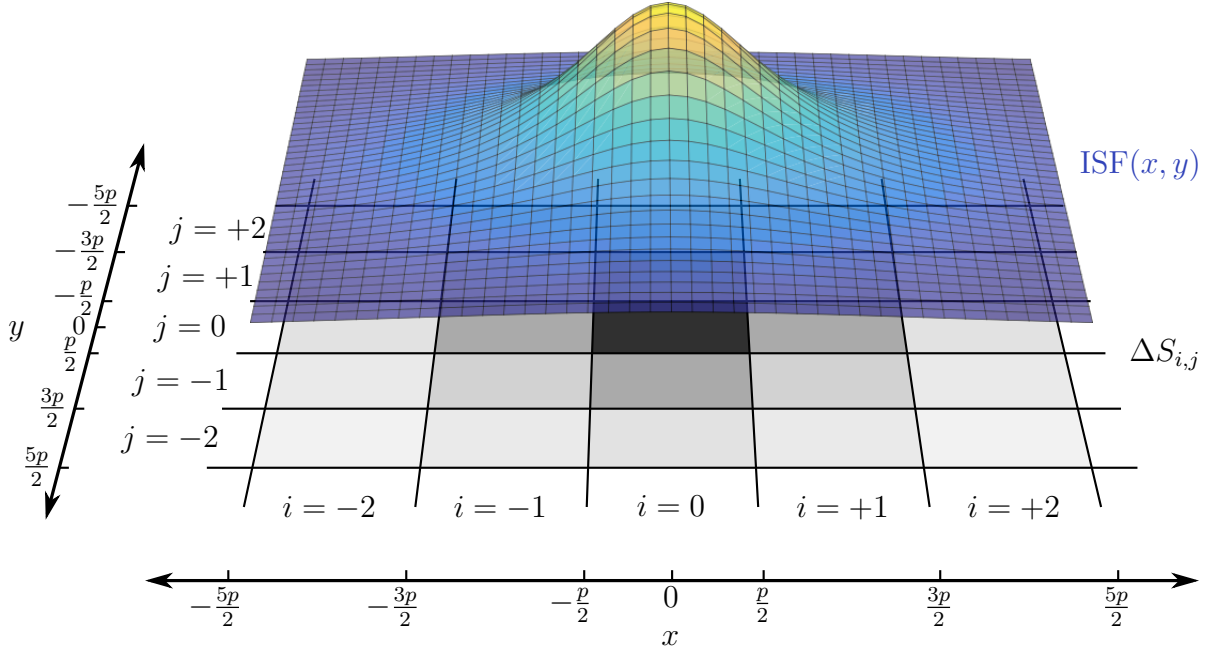
Figure 4.2: Diagram illustrating signal spread in a scintillator. The x-rays incident over the entire region above the middle pixel $(i = j = 0)$ result in a signal that is spread once it reaches the detector plane, represented by the ISF. This signal will eventually be discretized into pixels, each with a resulting value $\Delta S_{i,j}$.

frequency image with normal noise will reduce the image's standard deviation by a factor of $\sim (2\sigma_G\sqrt{\pi})$[47].

The standard deviation of signals generated by a monoenergetic x-ray source can now be updated to include scintillator blur as

$$\sigma_s \approx \frac{\sigma'_s}{2\sigma_G^s\sqrt{\pi}} \qquad\qquad \sigma_h \approx \frac{\sigma'_h}{2\sigma_G^h\sqrt{\pi}} \qquad\qquad (4.12)$$

where σ_G^s and σ_G^h are the standard deviations for the fitted Gaussian kernels of $\Delta S'$ for the expected soft tissue and iodinated vessel or nodule calcification signals, respectively.

As previously mentioned, this treatment is only applicable to the case of a monoenergetic source. However, it can be easily expanded to any source spectrum by first defining an energy-dependent $\sigma_G(E)$, which, at every energy E, would represent the σ_G obtained through this process using a pencil beam of that energy. Full polyenergetic signal variances

for $\tilde{S}_s$ and $\tilde{S}_h$ can be obtained by including the continuous $\sigma_G^2(E)/4\pi$ as part of the integrand in Equations (4.6) and (4.7). Put differently, the blurred pixel variance for each signal can now be estimated using these fitted $\sigma_G(E)$ values as

$$\sigma_s^2 = \frac{A}{4\pi} \int_0^\infty \Phi(E)e^{-\mu_s(E)t_s}\eta(E)\bar{Q}_{CsI}^2(E)\sigma_G^{-2}(E,t_{CsI},p)dE, \tag{4.13}$$

$$\sigma_h^2 = \frac{A}{4\pi} \int_0^\infty \Phi(E)e^{-\mu_s(E)(t_s-t_h)-\mu_h(E)t_h}\eta(E)\bar{Q}_{CsI}^2(E)\sigma_G^{-2}(E,t_{CsI},p)dE. \tag{4.14}$$

4.2 Extension to Three-Layer Detector

It is now possible to take Equations (4.1), (4.2), (4.13) and (4.14) and expand the developed analytical model to the proposed three-layer detector. Doing so requires simply to include the attenuation that the top layers will have on the x-rays reaching the bottom ones, and considering the difference in quantum efficiencies for each sensor due to their individual scintillator thicknesses. The mean and variance of each layer signals are denotes as $\bar{S}_{i,j}$ and $\sigma_{i,j}^2$, respectively. i represents the detector layer and can take the values of t, m or b for top, middle and bottom layer. j refers to the x-ray path of interest with a value of s representing the soft-tissue-only path and one of h symbolizing the path that goes through the high-attenuation-coefficient object of interest.

The signal means can be calculated using

$$\bar{S}_{t,s} = A \int_0^\infty \Phi(E)e^{-\mu_s(E)t_s}\eta_t(E)\bar{Q}_{CsI}(E)dE \tag{4.15}$$

$$\bar{S}_{t,h} = A \int_0^\infty \Phi(E)e^{-\mu_s(E)(t_s-t_h)-\mu_h(E)t_h}\eta_t(E)\bar{Q}_{CsI}(E)dE \tag{4.16}$$

$$\bar{S}_{m,s} = A \int_0^\infty \Phi(E)e^{-\mu_s(E)t_s}(1-\eta_t(E))\eta_m(E)\bar{Q}_{CsI}(E)dE \tag{4.17}$$

$$\bar{S}_{m,h} = A \int_0^\infty \Phi(E)e^{-\mu_s(E)(t_s-t_h)-\mu_h(E)t_h}(1-\eta_t(E))\eta_m(E)\bar{Q}_{CsI}(E)dE \tag{4.18}$$

$$\bar{S}_{b,s} = A \int_0^\infty \Phi(E)e^{-\mu_s(E)t_s}(1-\eta_t(E))(1-\eta_m(E))\eta_b(E)\bar{Q}_{CsI}(E)dE \tag{4.19}$$

40

$$\bar{S}_{b,h} = A \int_0^\infty \Phi(E) e^{-\mu_s(E)(t_s - t_h) - \mu_h(E) t_h} (1 - \eta_t(E))(1 - \eta_m(E))\eta_b(E)\bar{Q}_{CsI}(E)dE \quad (4.20)$$

where $\eta_i = 1 - e^{-\mu_{CsI}(E) t_i}$ are the layers' quantum efficiencies.

Meanwhile, their respective variances will also need to account for the detector design, and can be calculated with

$$\sigma_{t,s}^2 \approx \frac{A}{4\pi} A \int_0^\infty \Phi(E) e^{-\mu_s(E) t_s} \eta_t(E)\bar{Q}_{CsI}^2(E)\sigma_G^{-2}(E, t_t, p)dE \quad (4.21)$$

$$\sigma_{t,h}^2 \approx \frac{A}{4\pi} \int_0^\infty \Phi(E) e^{-\mu_s(E)(t_s - t_h) - \mu_h(E) t_h} \eta_t(E)\bar{Q}_{CsI}^2(E)\sigma_G^{-2}(E, t_t, p)dE \quad (4.22)$$

$$\sigma_{m,s}^2 \approx \frac{A}{4\pi} \int_0^\infty \Phi(E) e^{-\mu_s(E) t_s} (1 - \eta_t(E))\eta(E)\bar{Q}_{CsI}^2(E)\sigma_G^{-2}(E, t_b, p)dE \quad (4.23)$$

$$\sigma_{m,h}^2 \approx \frac{A}{4\pi} \int_0^\infty \Phi(E) e^{-\mu_s(E)(t_s - t_h) - \mu_h(E) t_h} (1 - \eta_t(E))\eta_m(E)\bar{Q}_{CsI}^2(E)\sigma_G^{-2}(E, t_b, p)dE \quad (4.24)$$

$$\sigma_{b,s}^2 \approx \frac{A}{4\pi} \int_0^\infty \Phi(E) e^{-\mu_s(E) t_s} (1 - \eta_t(E))(1 - \eta_m(E))\eta_b(E)\bar{Q}_{CsI}^2(E)\sigma_G^{-2}(E, t_b, p)dE \quad (4.25)$$

$$\sigma_{b,h}^2 \approx \frac{A}{4\pi} \int_0^\infty \Phi(E) e^{-\mu_s(E)(t_s - t_h) - \mu_h(E) t_h}$$
$$(1 - \eta_t(E))(1 - \eta_m(E))\eta_b(E)\bar{Q}_{CsI}^2(E)\sigma_G^{-2}(E, t_b, p)dE \quad (4.26)$$

where $\sigma_G(E, t_{CsI}, p)$ represents the standard deviation of a Gaussian kernel fitted to the $\Delta S'$ of a monoenergetic exposure of energy E on a detector of scintillator thickness t_{CsI} and a pixel pitch p.

4.3 Combining the Images

Due to the multiple operational modes of the detector, several final images can be obtained from the three layers' signals. The found expressions for the expected mean and variance of these signals make it possible to also calculate these values for the combined images. The final expression will, of course, depend on the operational mode of the detector. This section will detail this mathematical analysis for the two main operational modes explored, but the extension of this model to other modes is also possible and can be straightforward.

4.3.1 Conventional Radiographic Detector Mode

In this mode, the final image obtained from the detector is simply an addition of the signal from all three layers. The means of these final signals, $\bar{S}_{CR,j}$, can hence be calculated simply as

$$\bar{S}_{CR,s} = \bar{S}_{t,s} + \bar{S}_{m,s} + \bar{S}_{b,s}$$
$$\bar{S}_{CR,h} = \bar{S}_{t,h} + \bar{S}_{m,h} + \bar{S}_{b,h}. \tag{4.27}$$

The corresponding noise at each section of the image can also be easily calculated using the additive property of variance for independent random variables. Since no cross-talk is expected between the different layers, each signal is considered independent from the other[48], and thus the final variances are simply given by Equation (2.10) as

$$\sigma_{CR,s}^2 = \sigma_{t,s}^2 + \sigma_{m,s}^2 + \sigma_{b,s}^2$$
$$\sigma_{CR,h}^2 = \sigma_{t,h}^2 + \sigma_{m,h}^2 + \sigma_{b,h}^2. \tag{4.28}$$

4.3.2 Dual-Energy Detector Mode

The interesting property of the proposed detector is its ability to function as a single-shot dual-energy sandwich detector. In this mode, the enhanced image is obtained by combining the images from the top and bottom layers through logarithmic subtraction. Due to the applications studied in this thesis, the DE image of interest is that with removed soft-tissue background contrast. Therefore, I define the DE signals, $\tilde{S}_{DE,j}$, as those calculated to obtain an image that enhances hard-tissue components by applying Equation (2.16). The resulting expected means are approximated using Equation (2.11) as

$$\bar{S}_{DE,s} \approx \ln\left(\bar{S}_{b,s}\right) - w \ln\left(\bar{S}_{t,s}\right)$$
$$\bar{S}_{DE,h} \approx \ln\left(\bar{S}_{b,h}\right) - w \ln\left(\bar{S}_{t,h}\right) \tag{4.29}$$

where the weighting factor w is calculated with Equation (2.18) as

$$w = \frac{\mu_s(E_H)}{\mu_s(E_L)}. \tag{4.30}$$

Since the energies reaching each detector encompass a large spectral range, E_H and E_L were chosen as the average energies reaching the bottom and top detector layers when no object is being imaged. These are essentially the effective x-ray energies reaching each layer, and can be calculated using

$$E_L = \frac{\int_0^\infty \Phi(E)E\,dE}{\int_0^\infty \Phi(E)\,dE}, \tag{4.31}$$

$$E_H = \frac{\int_0^\infty \Phi(E)(1-\eta_t(E))(1-\eta_m(E))E\,dE}{\int_0^\infty \Phi(E)(1-\eta_t(E))(1-\eta_m(E))\,dE}. \tag{4.32}$$

It is also now possible to approximate the noise in the enhanced DE image for both signal types by applying Equation (2.12) to each term of Equation (4.29) and combining them through simple addition as per Equation (2.10). The resulting calculations and approximated variances are as follows

$$
\begin{aligned}
\sigma_{DE,s}^2 &\approx \left(\frac{d}{dx}\ln(x)\Big|_{x=\bar{S}_{b,s}}\right)^2 Var\{\tilde{S}_{b,s}\} + \left(\frac{d}{dx}\left(-w\ln(x)\right)\Big|_{x=\bar{S}_{t,s}}\right)^2 Var\{\tilde{S}_{t,s}\} \\
&\approx \frac{1}{\bar{S}_{b,s}^2}\sigma_{b,s}^2 + w^2\left(\frac{1}{\bar{S}_{t,s}^2}\sigma_{t,s}^2\right)
\end{aligned}
\tag{4.33}
$$

$$\sigma_{DE,h}^2 \approx \frac{1}{\bar{S}_{b,h}^2}\sigma_{b,h}^2 + w^2\left(\frac{1}{\bar{S}_{t,h}^2}\sigma_{t,h}^2\right)$$

4.4 Calculating Merit

4.4.1 Signal Difference and Noise

Determining the quality of an image can be a very complex task. The very fact that the final use of medical images are to be observed by a radiologist as a tool to aid in a diagnosis or treatment makes any possible mathematical metric to describe image quality an estimate at best. However, given the immense resources necessary for building a detector with a specific set of design parameters and performing a receiver operating characteristic

43

analysis[49], it is necessary to use a mathematical characterization of the images to optimize a newly proposed design.

A common metric to characterize the value of a radiographic image is the Signal Difference to Noise Ratio[24, 32, 50, 51]. It applies to those image types where the detectability of a particular object in a background is the desired objective, which fits exactly with the applications targeted by the detector designed proposed in this work. A simple example of this type of image is shown in Figure 4.3, where, while it might be trivial for an observer to determine the presence or absence of an object, the challenge of quantifying the ease of detecting the object becomes apparent.
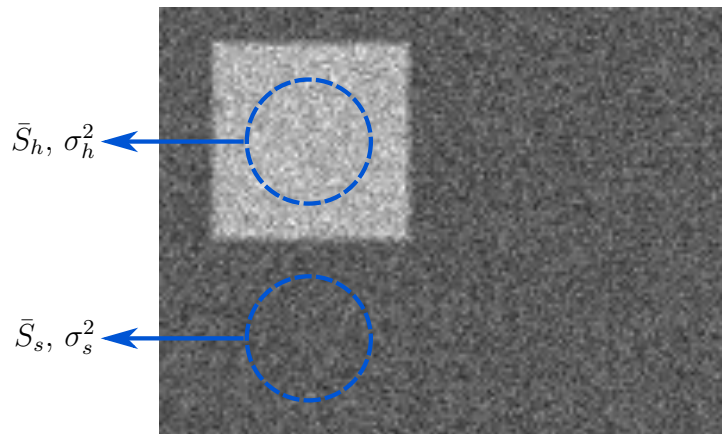
Figure 4.3: Example of a radiographic image containing a high-attenuation coefficient object of interest in a constant soft-tissue background. The pixels corresponding to each signal type that are used to calculate mean and variance are indicated.

SDNR aims to solve this and quantify the ability of an object to stand out to the observer by analyzing the contrast between the object of interest and its background with relation to the general image noise. In our applications, this background is formed by the soft tissue surrounding either an iodinated vessel or a nodule calcification. The contrast between these two tissue types is defined as the Signal Difference (SD) between two pixels located fully in either one of the paths of interest, and can be calculated simply with

$$\text{SD} = S_h - S_s. \tag{4.34}$$

To capture the negative effect that noise in both regions of the image will have on the ability to easily visualize the object, SDNR is defined as the mean of this Signal Difference divided by the square root of the sum of the variances corresponding to both tissue types. This definition makes for a parameter that can evaluate the detectability of an object embedded in its noisy background, and can be written mathematically as

$$\text{SDNR} = \frac{\overline{\text{SD}}}{\sqrt{\sigma_s^2 + \sigma_h^2}}. \tag{4.35}$$

Since this definition of SDNR applies to single images, it is natural to expand its expression to apply to the two types of combined images that are possible with the proposed detector. First, for a conventional radiographic image that is formed by simply adding all layers, the SDNR can be calculated as

$$\begin{aligned}
\text{SDNR}_{CR} &= \frac{\bar{S}_{CR,h} - \bar{S}_{CR,s}}{\sqrt{\sigma_{CR,s}^2 + \sigma_{CR,h}^2}} \\
&= \frac{\bar{S}_{t,s} + \bar{S}_{m,s} + \bar{S}_{b,s} - \bar{S}_{t,h} - \bar{S}_{m,h} - \bar{S}_{b,h}}{\sqrt{\sigma_{t,s}^2 + \sigma_{m,s}^2 + \sigma_{b,s}^2 + \sigma_{t,h}^2 + \sigma_{m,h}^2 + \sigma_{b,h}^2}}.
\end{aligned} \tag{4.36}$$

Next, this process can be repeated for the DE enhanced image, for which the SDNR can be approximated using the Taylor expansion approximation from Equations (2.11) and (2.12) as

$$\text{SDNR}_{DE} = \frac{\bar{S}_{DE,h} - \bar{S}_{DE,s}}{\sqrt{\sigma_{DE,s}^2 + \sigma_{DE,h}^2}}$$

$$\approx \frac{\ln\left(\bar{S}_{b,h}\right) - w\ln\left(\bar{S}_{t,h}\right) - \left[\ln\left(\bar{S}_{b,s}\right) - w\ln\left(\bar{S}_{t,s}\right)\right]}{\sqrt{\frac{1}{\bar{S}_{b,s}^2}\sigma_{b,s}^2 + w^2\left(\frac{1}{\bar{S}_{t,s}^2}\sigma_{t,s}^2\right) + \frac{1}{\bar{S}_{b,h}^2}\sigma_{b,h}^2 + w^2\left(\frac{1}{\bar{S}_{t,h}^2}\sigma_{t,h}^2\right)}} \tag{4.37}$$

$$\approx \frac{\ln\left(\frac{\bar{S}_{b,h}}{\bar{S}_{b,s}}\right) - w\ln\left(\frac{\bar{S}_{t,h}}{\bar{S}_{t,s}}\right)}{\sqrt{\left(\frac{1}{\bar{S}_{b,h}^2}\sigma_{b,h}^2 + \frac{1}{\bar{S}_{b,s}^2}\sigma_{b,s}^2\right) + w^2\left(\frac{1}{\bar{S}_{t,h}^2}\sigma_{t,h}^2 + \frac{1}{\bar{S}_{t,s}^2}\sigma_{t,s}^2\right)}}.$$

4.4.2 Figure of Merit

While SDNR is a good single metric to evaluate the quality of an image, it is easy to see its one limitation when employing it for the optimization of an imaging system. Given that SD will increase as the total exposure used to create the image increases, solely following SDNR will lead to favouring certain configurations that result in higher patient dosages. Parameters such as the x-ray tube voltage might be pushed too high, or the source filtration too low, if the maximization of SDNR is done blindly, resulting in configurations that are detrimental to the patient. Clearly, a metric that takes into account the amount of ionizing radiation that the patient is subjected to during the image exposure would be a more ideal parameter to abide by for optimization.

In developing such a metric, I begin by calculating the amount of radiation that a patient is given in order to obtain one image. This exposure, X (measured in röntgen or R), is defined as the total energy deposited in air during the imaging process[52, 53] and can be calculated using

$$X = \frac{C_R}{\bar{W}_{air}} \int_0^\infty \Phi(E)E\left(\frac{\mu_{en}(E)}{\rho}\right)_{air} dE \tag{4.38}$$

where $C_R \cong 6.201 \times 10^{-10}\,\mathrm{R\,g\,J/(keV\,C)}$ is a unit conversion factor, $\bar{W}_{air} \cong 33.97\,\mathrm{J/C}$ is the energy required to be deposited in air for the production of one ion pair averaged across the diagnostic energy range, and $(\mu_{en}(E)/\rho)_{air}$ is the mass energy-absorption coefficient of air at energy E. Note that most consequences of modifying x-ray tube parameters are accounted for in Equation (4.38) by the beam spectrum, $\Phi(E)$, which will change as these parameters change. It is important to note that $\Phi(E)$ is not the normalized x-ray fluence of the produced x-ray beam, but rather the number of photons per square centimetre.

Using this value, we can finally define a single-valued figure of merit (FoM) that will measure the quality of an image while being independent of patient exposure. Given that SDNR will increase with the square root of exposure[54], it is possible to define such an FoM by simply dividing SDNR by this factor, or

$$\mathrm{FoM} = \frac{\mathrm{SDNR}}{\sqrt{X}}. \tag{4.39}$$

This FoM will therefore not be biased towards higher-exposure configurations and allow for the comparison of different x-ray tube setups.

It is now possible to use this metric to quantify the performance of a detector as either a conventional radiography imager or a dual-energy detector by including the respective SDNR values of the final enhanced images in its calculation as

$$\mathrm{FoM}_{CR} = \frac{\mathrm{SDNR}_{CR}}{\sqrt{X}} \qquad\qquad \mathrm{FoM}_{DE} = \frac{\mathrm{SDNR}_{DE}}{\sqrt{X}}. \tag{4.40}$$

Chapter 5

Dual-Energy Mode Optimization

While the general design of the proposed detector has been established, it is still necessary to determine the ideal values of all the design parameters. To find the best configuration, these values are chosen such that the highest possible figure of merit is obtained in the resulting enhanced images.

Since this three-layer detector is meant to compete with established Dual-Energy systems first (and have the additional conventional radiographic image at no extra time or exposure cost second), the parameter optimization aims to maximize the detector's DE performance. The simplicity of the conventional radiography image also means that its optimization process is less complex, and that a sufficient image will be obtained for all reasonable parameter values. It is hence unnecessary to optimize detector parameters for this operational mode. Therefore, I chose to focus on FoM_{DE} when determining the ideal imaging system configuration. This chapter will detail the optimization process done through the application of the developed analytical model and the corroboration of the results obtained through complex Monte Carlo ray-tracing simulations.

5.1 Optimization Using Analytical Model

Using the analytical model developed in Chapter 4, the ideal detector configuration can be found by computing FoM_{DE} for all possible reasonable values of the parameters. The aspects of the imaging system that were optimized are those pertaining to the x-ray tube

source—including both its peak voltage and filtering—and the thicknesses of the middle and top layers' scintillators. These parameters and the possible ranges and values considered for them throughout the optimization process are summarized below in Table 5.1. The chosen ranges were selected by considering current FPD, scintillator and x-ray tube technologies commercially available and typical for conventional radiography systems.

Symbol	Definition	Range
kVp	Peak x-ray tube voltage	$50\,\mathrm{kV}$ to $140\,\mathrm{kV}$
t_f	Thickness of source filtering	$0\,\mathrm{mm}$ to $5\,\mathrm{mm}$
	Source filtering material	Al, Cu, Rh, Mo, Ag, Sn
t_t	Thickness of top scintillator	$50\,\mathrm{\mu m}$ to $300\,\mathrm{\mu m}$
t_m	Thickness of middle scintillator	$100\,\mathrm{\mu m}$ to $800\,\mathrm{\mu m}$

Table 5.1: Detector and x-ray source parameters and ranges studied to optimize the theoretical performance of the proposed detector imaging system.

It quickly becomes clear that the optimal set of detector parameters will not only heavily depend on the application of choice, but also on the particulars of the object of interest being detected. For this reason, typical objects with a wide range of parameter values were studied in the optimization process in order to represent those objects that are normally encountered in the chosen imaging applications. For the pulmonary nodule assessment application, the possible thickness of a calcification was varied in the range specified in Table 5.2. This table also shows the range studied for the mass loading of a iodinated vessel when considering the coronary angiography application.

This last parameter, I_{ml}, is particularly interesting because it is a way to collapse two characteristics of an iodinated vessel into one: its thickness and the iodine concentration in blood. It is defined as the total amount of iodine that an x-ray beam would encounter per unit area when transversely passing through the vessel[55], and can be calculated simply as

$$I_{ml} = \rho_I t_v, \tag{5.1}$$

where ρ_I is the density of iodine in blood and t_v is the thickness of the vessel. Since the analytical model developed only requires the final level of x-ray attenuation of an

Symbol	Definition	Range
t_c	Thickness of calcification	$1\,\text{mm}$ to $5\,\text{mm}$
I_{ml}	Vessel's iodine mass loading	$10\,\text{mg/cm}^2$ to $75\,\text{mg/cm}^2$

Table 5.2: Application-specific parameters and their ranges considered when optimizing the theoretical performance of the proposed detector. I_{ml} is varied when analyzing detectability of iodinated vessels in coronary angiography, while t_c when optimizing the system for calcification detection in pulmonary nodules.

object to perform calculations, any parameter that succinctly expresses this numerically is appropriate. Iodine mass loading is more appropriate for such a purpose because it can simplify contrast agent dilution calculations and will make the dependency on application parameters much simpler.

Several characteristics of the imaging system were not allowed to change in the optimization process and were fixed a priori. The first is the target material in the x-ray tube source, for which tungsten was selected due to its ubiquity in radiography systems[3], particularly those tailored for chest x-rays. The next fixed characteristics are the scintillator material and structure of all the three detector layers. I chose Thallium-doped Cesium Iodide as the scintillating material due to its maturity, availability and ability to be grown structurally[13]. This material is also attractive due to its common and established integration with FPD technology, which makes it a natural choice for a detector that required three FPDs and three scintillating screens. It was assumed to be grown structurally on top of each TFT layer through a vapour deposition process. When performing numerical calculations, the packing efficiency of the CsI:Tl columnar scintillator was taken to be $75\,\%$, as reported in previous works[45].

Further constrains were imposed on the detector itself. First, the pixel pitch p was set to $100\,\mu\text{m}$, as it is a reasonable state-of-the-art pixel size for an a-Si FPD. Second, the bottom detector layer is meant to absorb as many as possible of the high-energy x-rays that reach it without introducing too much signal spread, and thus its scintillator thickness t_b was not varied but rather set to a reasonable high-end limit of $500\,\mu\text{m}$ imposed by fabrication and blurring constraints.

In these calculations, the x-ray spectrum of a tungsten anode tube was computed for different kVp values using Spektr[56], a Matlab$^{\text{TM}}$ implementation of the TASMIP[57] (tungsten anode spectral model using interpolating polynomials) empirical model of x-ray tube spectra, since this model has proven to be one of the most accurate in its predictions[58]. The source filtering with different materials and thicknesses t_f was computed using the built-in filtering capabilities of Spektr. All mass attenuation and mass energy-absorption coefficients, as well as all material and tissue densities, were obtained from the National Institute of Standards and Technology (NIST) measurement compilation[21].

As mentioned previously in Section 4.1.2, no mathematical algorithm exists to calculate the expected signal spread due to a certain set of scintillator and x-ray parameters. Instead, I developed a computational model to be able to quickly calculate the resulting scintillator blur for a specific parameter set that is based on simulation results.

First, Monte Carlo ray-tracing simulations were performed using the hybrid MANTIS simulation package (see Section 5.2) to obtain $\text{PRF}(x, y, E)$ values. These simulations consisted of recording the intensity of optical light quanta that reached the detector plane when a monoenergetic pencil beam source was shone in the centre of a simulated scintillating screen. Several model screens of thicknesses in the range from $50\,\mu\text{m}$ to $800\,\mu\text{m}$ at $10\,\mu\text{m}$ increments were used, all of which were modeled as highly structured CsI:Tl scintillators. The energy of the monoenergetic beams were varied from $10\,\text{keV}$ to $150\,\text{keV}$ at $5\,\text{keV}$ increments to obtain a value of the PRF across the entire diagnostic x-ray spectrum. Note that while it was necessary to discretize the PRF into square pixels due to the nature of the simulation program, very small detector pixel pitches were used to approximate a continuous PRF function as best as possible.

Next, using the simulated PRF function values at different energies and scintillator thicknesses, the analytical process described in Section 4.1.2 was followed to obtain the corresponding standard deviation of a fitted Gaussian kernel. Firstly, the respective $\Delta S_{i,j}$ functions were computed for all the PRFs using pixel pitch values in the range of $50\,\mu\text{m}$ to $150\,\mu\text{m}$ at $10\,\mu\text{m}$ increments. From that, the normalized $\Delta S'_{i,j}$ functions were calculated and fitted with a Gaussian kernel.

With this method, a value for the blurring that will result from a specific x-ray energy, scintillator thickness and pixel pitch was obtained in the form of $\sigma_G(E, t_{CsI}, p)$. However, these standard deviations were only available at the discrete parameter values chosen at the time of running the simulations and computations. To obtain a continuous function

(a)

(b)
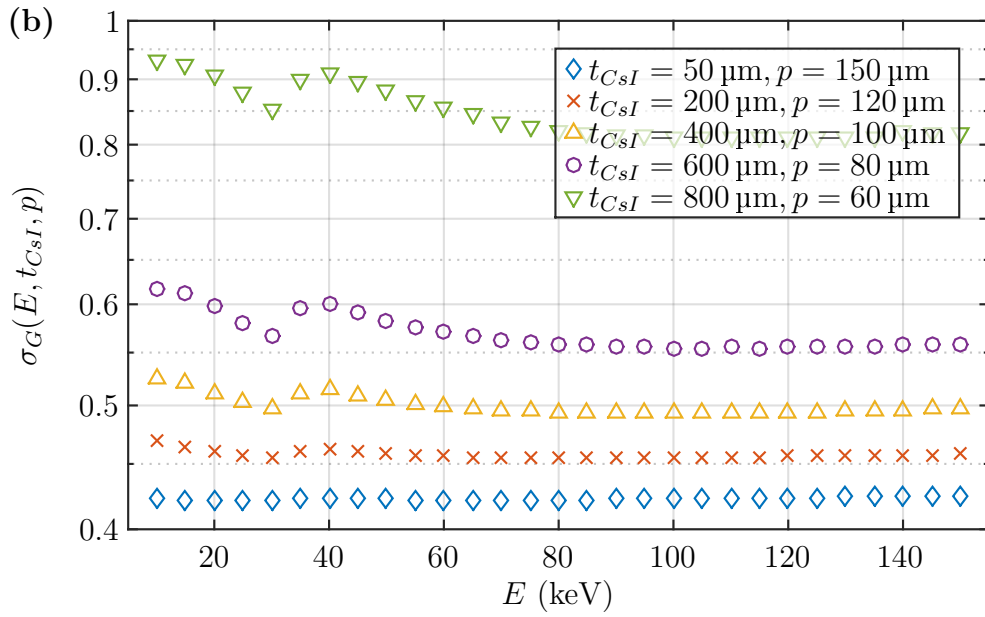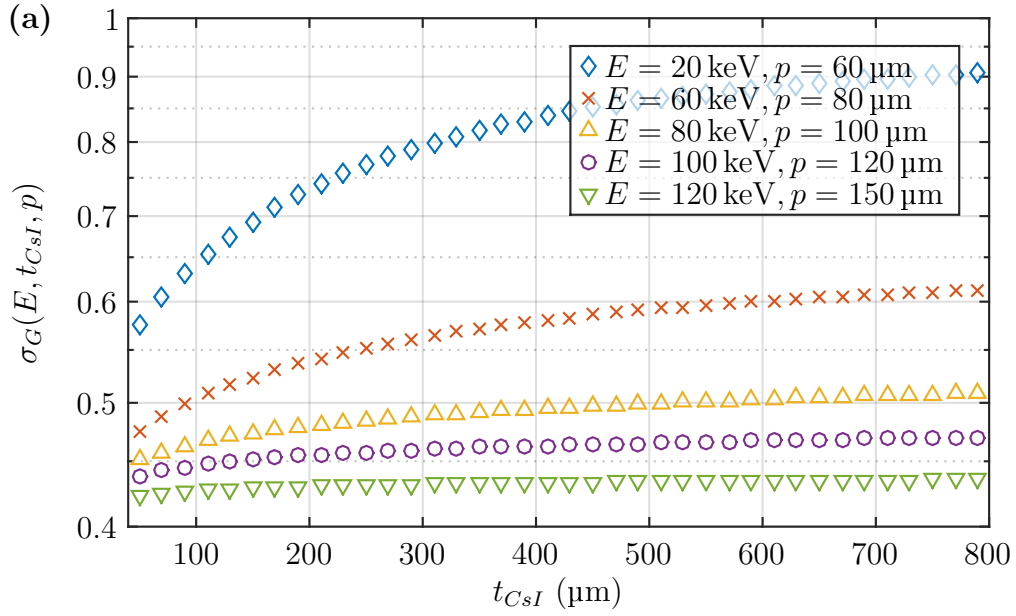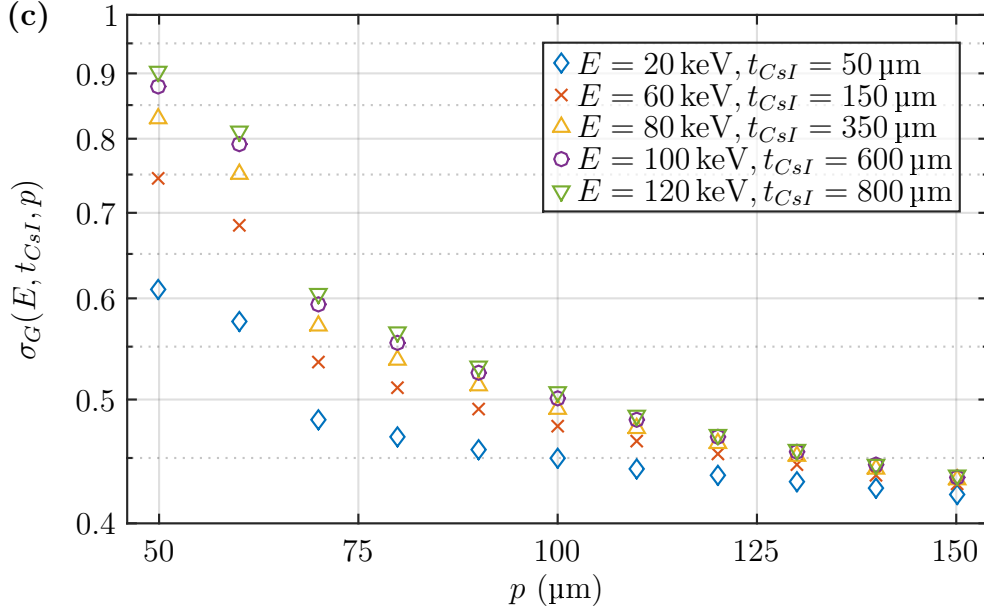
Figure 5.1: Calculated values of the standard deviation $\sigma_G(E, t_{CsI}, p)$ of the fitted Gaussian kernel used to model $\Delta S(E, t_{CsI})$ and ultimately allow for fast calculations of scintillator-induced image blur. A representative sample of the calculated values are shown as a function of **(a)** scintillator thickness, **(b)** energy of the input monoenergetic beam, and **(c)** detector pixel pitch.

of $\sigma_G(E, t_{CsI}, p)$ that would allow for a quick calculation of blur according to these input parameters, the discrete values were then interpolated using natural neighbour interpolation. Figure 5.1 shows a subset of these discrete results to demonstrate that σ_G is a fairly well-behaved and thus these interpolations were sensible.

With that, using the developed analytical model presented above, the proposed detector design was optimized to obtain the best possible Dual-Energy enhanced image as measured by the FoM$_{DE}$. The results for this optimization and further validation of its results are presented in Chapter 6 below.

5.2 Monte Carlo Validations

The final optimization results from the analytical model developed above were validated using computer software to simulate the three-layer detector and its imaging abilities when applied to the studied applications. These were carried out using the software package hybridMANTIS[59], a Monte Carlo tool meant for modeling indirect x-ray detectors with columnar structured scintillators as its sensing layer. hybridMANTIS is an extension of the package MANTIS[60] (or Monte carlo x-rAy electroN opTical Imaging Simulation), an imaging system simulation tool that can model the transport of x-rays, electrons in matter and optical photons in the scintillator. MANTIS is itself based on the simulation tool PENELOPE[61], and uses its geometry system, x-ray and electron transport, and source modeling, but extends on the optical photon transfer capabilities to better model a columnar scintillator structure. In MANTIS, the process of x-rays interacting in the scintillator and transferring their energy to generated optical photons is simulated by computing a probabilistic model of these interactions event by event. While this makes it a very powerful tool, it does mean that it requires large computational resources. hybridMANTIS attempts to reduce computational times by performing these calculations using a hybrid CPU-GPU technique, hence the "hybrid" in its name.

Using hybridMANTIS, the optimized imaging system for the proposed three-layer detector was simulated with the optimal parameters for each of the target applications. Each detector layer was modeled as a structured CsI block of specific thickness, immediately followed by a thin 1 μm layer of Aluminum used to simulate the flat-panel thin film transistors, and then by a 0.5 mm glass layer representing the panel's substrate. A small 0.5 mm air gap was left in between each layer to best simulate the expected assembly constraints. With the resulting images obtained from these simulations, the FoM results from the analytical calculations could be verified. An example of the images obtained in these simulations and how they are combined in either detector mode is shown in Figure 5.2.

Each of the target applications required a simulation with a specific object geometry to be imaged. For the coronary angiography application, six individual blood vessels of increasing iodine mass loading I_{ml} were modeled as cuboids with a width and depth of 5 mm and infinite length. The cuboid material was set to a mixture of blood and the necessary amount of an iodine contrast medium molecule to result in the desired I_{ml} for each vessel. The composition of the blood used was as defined by the International Commision on Radiological Protection (ICRP) and as provided by NIST[62], the details of which are
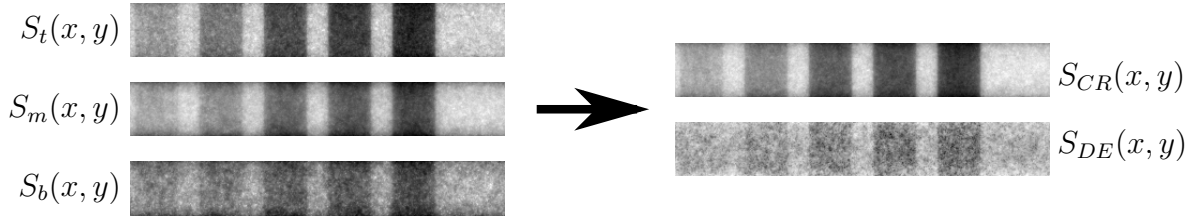
Figure 5.2: Example images of iodine vessels of increasing I_{ml} from left to right obtained with Monte Carlo simulations in hybridMANTIS. S_s and σ_s are obtained from the right-most part of the image. S_{CR} and S_{DE} are calculated using Equation (4.27) and Equation (4.29) respectively. Note that the enhanced S_{CR} presents a lower-noise image that any individual layer through the simple combination of their signals, and that while S_{DE} is the noisiest image, it will have the advantage of removing any contrast from the soft-tissue background.

shown in Table 5.3a. The iodine contrast agent modeled was Iopromide, as it is commonly used in radiographic and computed tomography studies. Its chemical composition was taken to be as defined by the PubChem Compound Database[63] as $C_{18}H_{24}I_3N_3O_8$. Most iodine contrast agents are, however, very chemically similar, and hence the results obtained using Iopromide will also apply to other available agents.

In the case of the pulmonary calcification detection application, five calcified nodules were simulated as cubes of increasing size t_c at 1 mm increments, and hence increasing total attenuation. Their material compositions were set to pure elemental calcium, but with a density equal to that of soft tissue as defined by ICRP.

For both imaging applications, these objects were placed in the centre of a 20 cm-thick slab of ICRP-defined soft tissue[62], the composition of which is shown in Table 5.3b. This effectively simulates the patient's surrounding soft tissue and provides the background signal for FoM$_{DE}$ calculations.

With this mentioned simulation setup, it was possible to obtain an FoM$_{DE}$ value for several discrete values of the application-specific parameters that encompass the entire studied range detailed in Table 5.2 by only obtaining one single set of images. Due to the limitations of hybridMANTIS, a new simulation was required for acquiring each layer's image. That is, three individual simulations were required to obtain one single set of images. While this would remove any noise correlations between the images, it does not pose a problem as the signals of the different layers are expected to be independent regardless[48].

Element	Fraction
H	0.101866
C	0.100020
N	0.029640
O	0.759414
Na	0.001850
Mg	0.000040
Si	0.000030
P	0.000350
S	0.001850
Cl	0.002780
K	0.001630
Ca	0.000060
Fe	0.000460
Zn	0.000010

(a) Composition of ICRP Blood. Its density is taken to be $1.06\,\mathrm{g/cm^3}$.

Element	Fraction
H	0.104472
C	0.232190
N	0.024880
O	0.630238
Na	0.001130
Mg	0.000130
P	0.001330
S	0.001990
Cl	0.001340
K	0.001990
Ca	0.000230
Fe	0.000050
Zn	0.000030

(b) Composition of ICRP Soft Tissue. Its density is taken to be $1.00\,\mathrm{g/cm^3}$.

Table 5.3: Detailed elemental composition of the materials used for simulations. Element fractions are reported by weight. Data obtained from NIST[62].

Chapter 6

Results and Discussion

6.1 Optimization Results

Optimizing the proposed three-layer detector using the analytical model presented in Chapter 4 is by nature a multivariate process. To be able to perform this optimization in reasonable computing times, I developed a nonlinear regression algorithm using the MATLAB$^{\mathrm{TM}}$ software package. While all the optimized parameter values were therefore obtained simultaneously, they are presented sequentially in this section for the sake of clarity.

It is important to note that where plots of the effects that the variation of a particular variable has on FoM_{DE} are presented, all other parameters are kept at their optimized value. In other words, the remaining parameters are not re-optimized for each value the current variable takes but rather are maintained in their final optimal configuration. Doing this allows for a better understanding of the effects that each individual variable has on the chosen figure of merit.

6.1.1 Source and Its Filtering

The first element of the imaging system that was optimized is the x-ray source and its filtration elements. The property that will have the largest impact on the chosen figure of merit will be the peak tube voltage, since it will determine the spectral width of the x-ray beam and hence the possible energy separation between each detector layer. Increasing

57

the kVp resulted in a steady increase of the FoM_{DE}, as is shown for both application cases in Figure 6.1. Therefore, the source should be operated at the highest kVp possible. Since commercial x-ray tube sources have operational constrains on the tube voltage, a reasonable upper limit for tungsten-anode sources was chosen and so kVp was set to 120 kV for all further simulations.
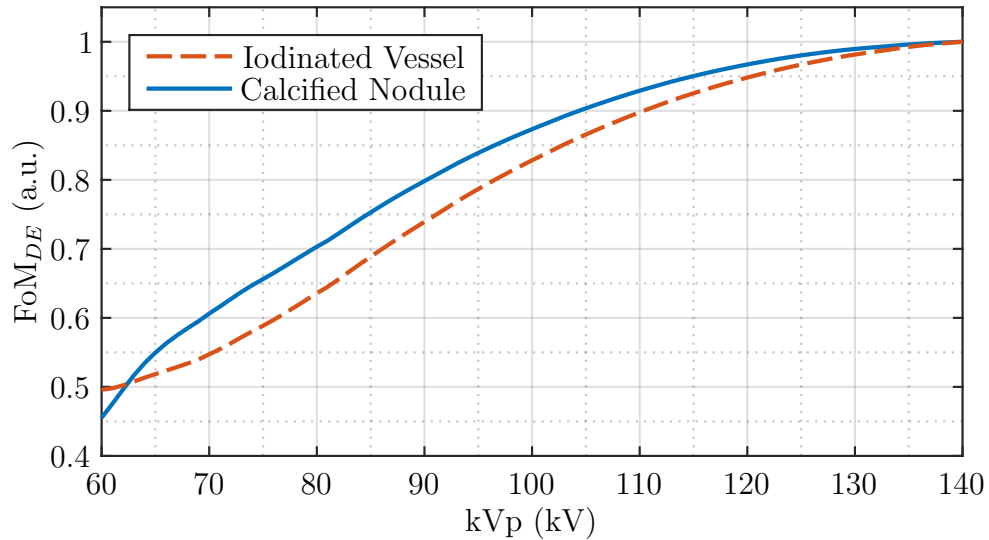
Figure 6.1: Effects of x-ray source tube voltage on FoM_{DE} for a mid-range object of interest in each application considered. An iodinated vessel of $I_{ml} = 50\,\mathrm{mg/cm^2}$ was modeled for the coronary angiography application, while a calcified nodule of $t_c = 3\,\mathrm{mm}$ was used for the pulmonary radiography calculations.

The second set of parameters related to the x-ray source that were optimized are the filtration materials and their thicknesses. The two elements out of the six tested that were found to independently increase FoM the most were aluminum (Al) and copper (Cu). Figure 6.2a shows an example of the different positive effect of both filter elements. Adding Al filtering will result in a continuous FoM_{DE} increase but with diminishing returns at higher thicknesses, while the Cu effect will peak at $\sim 0.2\,\mathrm{mm}$ and decrease with higher filter thickness t_f. It is important to note that these two filtration benefits cannot be combined, but rather the optimization of one will remove almost all positive effects of the other. Thus, sole Al filtration becomes the obvious practical solution, since there is no need to precisely optimize t_f to achieve maximum benefit, but rather a better result
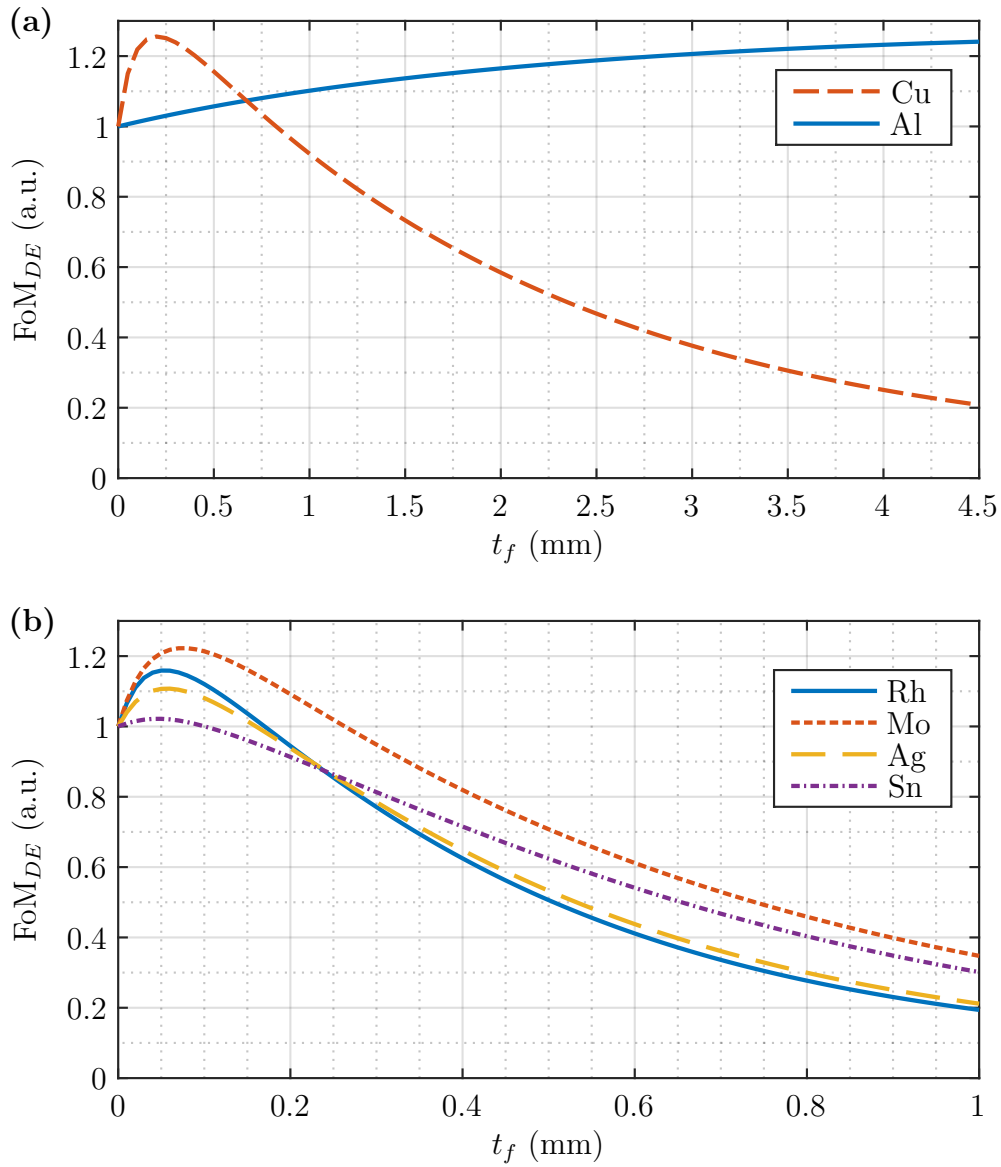
Figure 6.2: Effects of source filtering on FoM_{DE} for filter elements **(a)** Al and Cu, and **(b)** Rh, Mo, Ag and Sn. All models include a $0.1\,\text{mm}$ intrinsic Al filtering, as most commercial tungsten sources do so. While the same trends were observed for both of the applications studied throughout their entire parameter value ranges, both figures show the specific example of the detection of an iodinated vessel of $50\,\text{mg/cm}^2$ mass loading in $20\,\text{cm}$ of soft tissue.

can be achieved by simply increasing the thickness. Similarly to choosing kVp, a sensible maximum value of $t_f = 3\,\mathrm{mm}$ of Al was chosen for the optimized imaging system as a practical high-end limit and will be used in further calculations.

The remaining filter element materials studied were rhodium (Rh), molybdenum (Mo), silver (Ag) and tin (Sn). As can be seen in the example in Figure 6.2b, most of these presented a similar trend to Cu, but with less of a positive effect on FoM_{DE} and a narrower peak with a quicker decline. The scale of the abscissa must be noted as it is significantly different for both figures in Figure 6.2, which can lead to the wrongful impression that the effects of Cu and these four materials are similar in scale. In fact, the issue of precisely needing to optimize the filter thickness to obtain an FoM_{DE} improvement is magnified for these elements. As such, these elements do not present a good alternative to Al filtering, whose simpler function makes it the best candidate.

Several combinations of different thicknesses of all filter materials were also studied, but only minute FoM_{DE} improvement were found in the best of cases. The practicality of combining and simultaneously optimizing multiple filters is certainly not worth these small improvements, which could also be achieved by slightly increasing the Al thickness. Moreover, these increases are only possible when dealing with only one object of interest, and cannot be achieved for the entire range of the object attenuation that is expected for each application.

6.1.2 Scintillator Thicknesses

Perhaps the most important parameters that must be optimized are those pertaining to the detector itself, as these do not refer to the operation of the imaging system but rather to the fabrication step. Determining the ideal thickness of the scintillating material of each detector layer is key to building to best possible Dual-Energy imager. Since both scintillators must be thin enough to allow for x-rays to penetrate them and reach the next layers but thick enough to both harden the x-ray beam and absorb sufficient photons for the creation of a good image, finding the ideal value can be a challenge.

To find these optimal thicknesses, both t_t and t_m were allowed to independently vary along their respective ranges in the analytical model developed, while the source and filtration parameters were set to the optimized values mentioned above. The results of
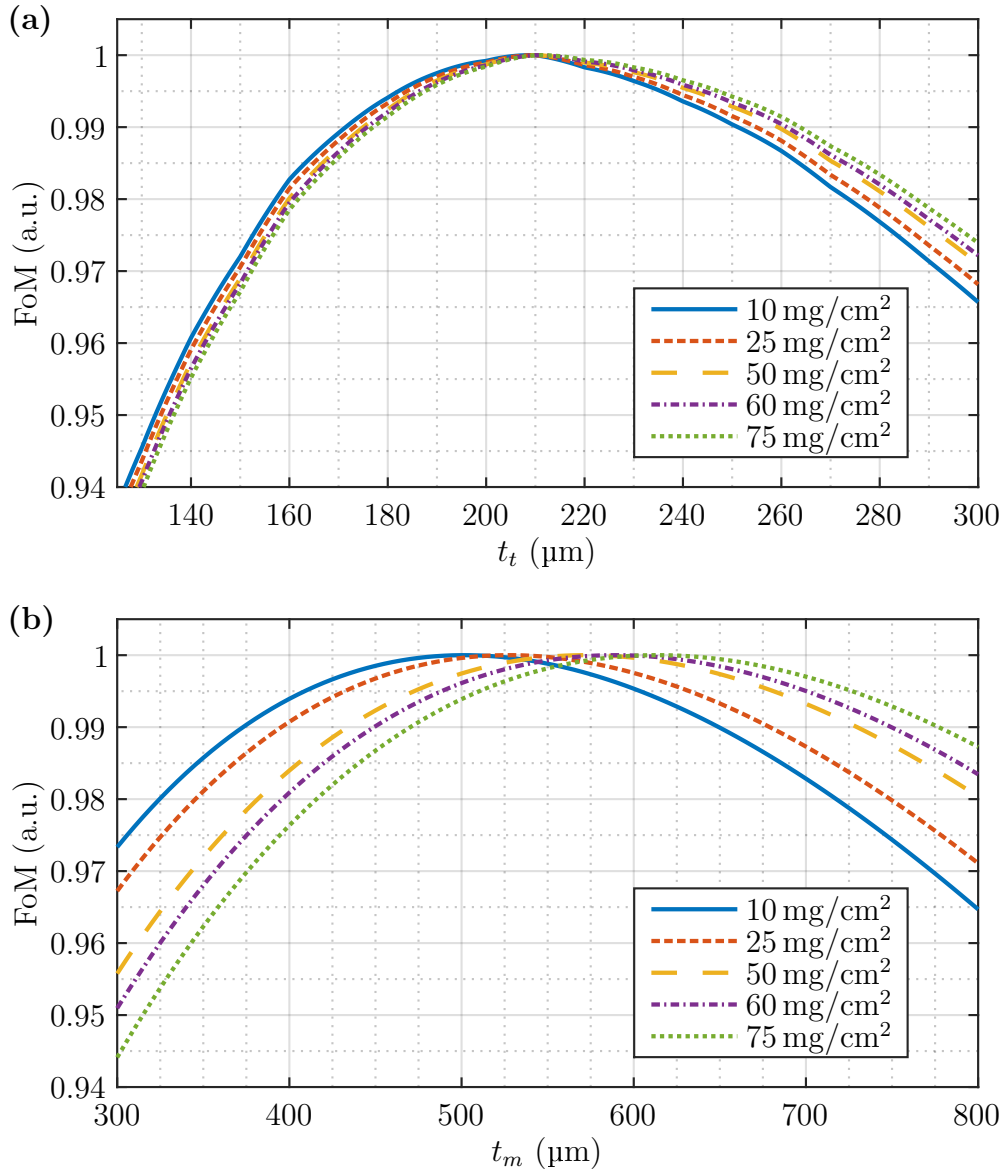
Figure 6.3: FoM_{DE} results when varying **(a)** top scintillator thickness and **(b)** middle scintillator thickness for iodinated vessel detection in coronary angiography at various I_{ml} values across the studied range. Each curve is independently normalized to its maximum value since a higher I_{ml} will intrinsically result in higher FoM_{DE} results. All other parameters are set to their ideal values for each individual curve displayed.

Figure 6.4: FoM$_{DE}$ results when varying **(a)** top scintillator thickness and **(b)** middle scintillator thickness for calcified nodule detection in pulmonary radiology at various t_c values across the studied range. Each curve is independently normalized to its maximum value since a higher t_c will intrinsically result in higher FoM$_{DE}$ results. All other parameters are set to their ideal values for each individual curve displayed.
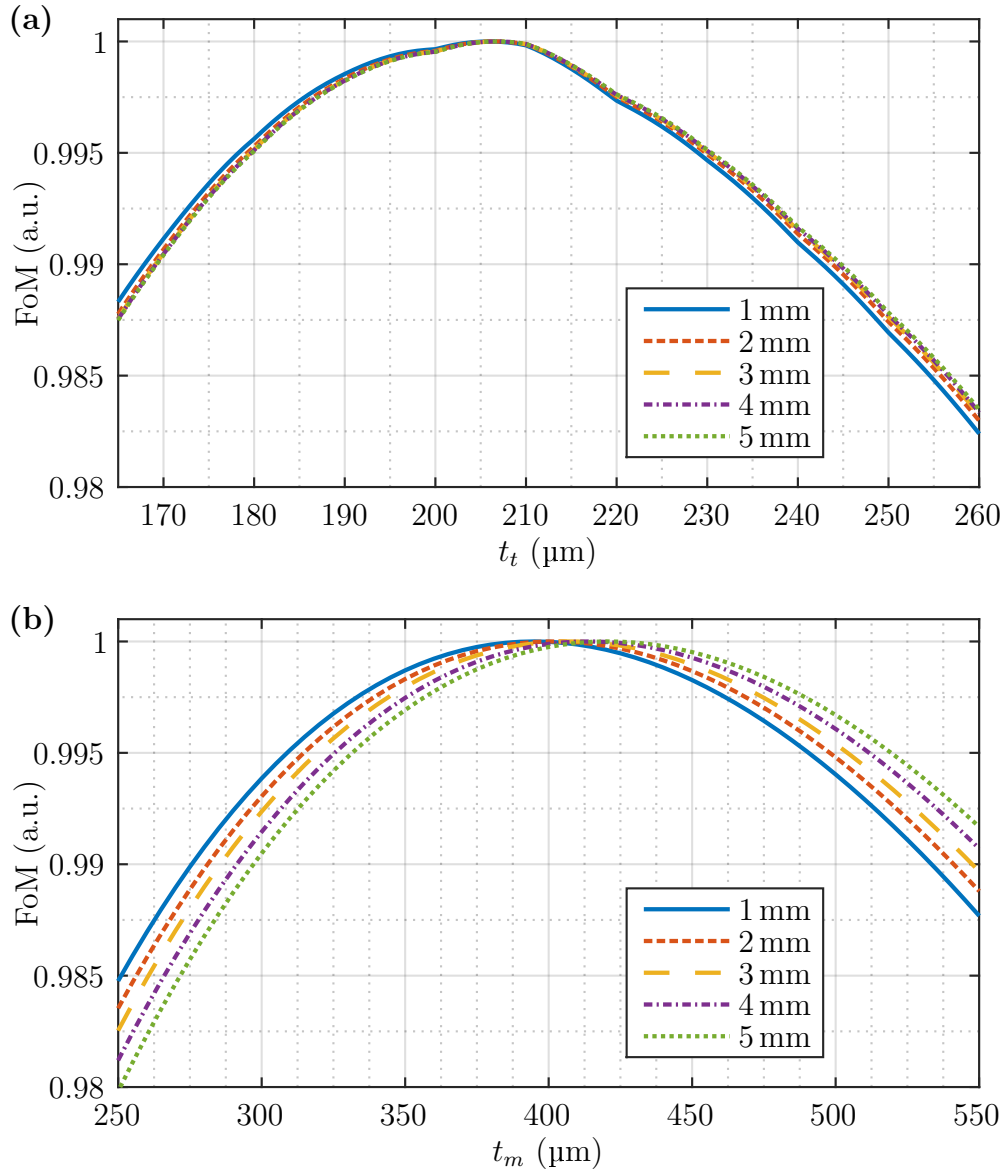
these simulations are shown in Figure 6.3 for the iodinated vessel detection application and in Figure 6.4 for the calcified pulmonary nodule detection application.

These figures show the heavy dependence that the optimal values for both thickness parameters will have on the attenuation of the object of interest—and hence on I_{ml} or t_c—, particularly when dealing with t_m. It clear from this that any application that spans the large ranges in I_{ml} or t_c as the ones studied in this work will require a detector that compromises on the values of these thicknesses to best suit the entire range. Put differently, given that the ideal scintillator thicknesses corresponding to every possible value of these application parameters cannot be chosen during detector fabrication, those that maximize the *mean* FoM$_{DE}$ across the whole range are considered the ideal ones.

In order to find the aforementioned compromised thickness values, I begun by calculating the optimized thicknesses for each one of the used discrete application parameter values. From there, it was possible to calculate a reasonable value for each thickness given the range these optimized values span. The results I deemed most appropriate for the parameter ranges I investigated were 210 µm and 560 µm for t_t and t_m respectively when considering the iodinated vessel visualization application, and 255 µm and 440 µm for calcified nodule detection. These results are also summarized in Table 6.1 below.

Iodinated Vessel			Calcified Nodule		
I_{ml} (mg/cm^2)	t_t (µm)	t_m (µm)	t_c (mm)	t_t (µm)	t_m (µm)
10	209	501	1	254	424
25	210	527	2	254	431
50	210	572	3	255	436
60	210	589	4	255	443
75	211	614	5	255	450
	210	**560**		**255**	**440**

Table 6.1: Optimized scintillator thicknesses for discrete values spanning the range of application parameters. Both applications are listed by their respective objects of interest. The last row shows in bold the chosen compromised values for the thicknesses.

63

6.1.3 Optimized Parameters Summary

With the optimization process developed above, the ideal values for each imaging system parameter became clear. While some reasonable real-world limits must be imposed on the bottom detector scintillator thickness, the x-ray tube peak voltage and the thickness of the aluminum filtration, the values that will result in the best possible DE enhanced image could be determined. Said values are summarized below in Table 6.2.

Object of Interest	kVp	t_t	t_m	t_f	Material
Iodinated Vessel	120 kV	210 µm	560 µm	3 mm	Aluminum
Calcified Nodule	120 kV	225 µm	440 µm	3 mm	Aluminum

Table 6.2: Summary of the optimized values of parameters pertaining to the proposed three-layer detector imaging system for each of the applications studied. Applications are listed by their object of interest.

The work presented here focused on two specific applications, and thus the ideal parameter values must only be considered to apply to them. However, through the analytical model developed, it should be possible to easily expand this work to any application that seeks to increase the detectability of a high-attenuation-coefficient object embedded in a cluttered soft-tissue background. Whether the ideal system parameters will be similar to those found for these applications remains to be seen.

6.2 Comparison with Other Dual-Energy Detectors

In order to evaluate the performance of the proposed detector as a DE imager, it is necessary to compare it with the two established Dual-Energy technologies detailed in Section 2.4.1. The first is a kVp switching single-layer detector, and the second is a single-shot dual-layer detector with a metal mid-filter. To fairly compare the three imager types, I developed modified versions of the presented analytical model that will apply to each detector individually and allow for the computation of their FoM_{DE} at specific parameter values. Note that this means that this comparison only applies to their functionality as a DE imager, and not to any other operational modes that the proposed detector is capable of.

6.2.1 kVp Switching

For the kVp switching imaging system, several modifications to the analytical model were necessary. First, it could be significantly simplified since the detector only has a sole flat-panel layer and hence only one scintillator layer. Its thickness, t_{CsI}, was allowed to vary in the 100 µm to 700 µm range during the optimization process.

Second, large modifications were needed due to the source spectral changes between the two exposures. Since the peak tube voltage must differ from one image to the next to obtain the HE and LE spectra, two parameters were defined: kVp_{LE} and kVp_{HE}. The former represents the peak tube voltage during the acquisition of the LE image and was optimized in the 20 kVp to 60 kVp range, while the later is the same voltage at the acquisition time of the HE image and was allowed to vary in the 60 kV to 140 kV range.

Not only will the spectral shape change between the two exposures, but the total number of x-ray photons generated in the beam will also not be equal. While this is determined by the tube current in practical scenarios, it was controlled in the model by allowing different exposures X during the acquisition of each image. Since FoM_{DE} is exposure-independent, it will not be affected by changes in the *total* patient exposure (that is, the sum of the exposures necessary to obtain the LE and the HE image), but it will be affected by their relative values. It is therefore possible to absorb these two parameters into a single one, the low-to-high exposure ratio, $X_{L:H}$. This parameter was optimized in the model by varying it from 0.1 to 10.

The results from this optimization process are shown below in Table 6.3. Note that, similarly to the optimization of the three-layer detector, certain maximum constraints were imposed on some parameters. Specifically, kVp_{HE} was capped at a reasonable maximum of 120 kV since increasing it showed constant FoM_{DE} improvements, and t_{CsI} was not allowed to grow further than 500 µm for blurring concerns. Interestingly, copper source filtration proved most advantageous for kVp switching, with a similar trend to that of Aluminum in the three-layer detector. Its thickness was therefore also set to a reasonable practical maximum of 3 mm.

Symbol	Definition	Ideal Value for Detection of	
		Iodinated Vessel	Calcified Nodule
kVp_{LE}	kVp during low-energy exposure	41 kV	37 kV
kVp_{HE}	kVp during high-energy exposure	120 kV	105 kV
t_f	Thickness of source filtering	3 mm	3 mm
	Source filtering material	Copper	Copper
$X_{L:H}$	Low-to-high-energy exposure ratio	1.5	1.7
t_{CsI}	Thickness of sole scintillator	500 µm	500 µm

Table 6.3: Parameters optimized in the analytical model for the kVp switching imaging system and their ideal values for both of the applications studied.

6.2.2 Dual-Layer Detector

Fewer modifications were necessary to develop a model for a conventional single-shot dual-layer detector that utilized a metal mid-filter. The main difference with the already described analytical model is that the middle layer, instead of being a flat-panel layer with a scintillator, is instead a metallic filter and will not be able to obtain a signal.

Two parameters were newly introduced that pertain to the mid-filter. The first is its material, which was tested using the same options as those used for source filtering: Al, Cu, Rh, Mo, Ag, and Sn. The second is the filter's thickness, t_{m-f}, which was investigated in the model along the range of 100 µm to 2000 µm.

Similar maximum constraints as before were imposed on the conventional dual-layer detector model. These include the established maximum of the x-ray tube voltage and filtration material thickness, which were set to 120 kVp and 3 mm respectively, and the thickness of the bottom layer's scintillator, which was capped at 500 µm. The results of these optimizations are detailed in Table 6.4 below. As expected by what is used by other dual-layer detectors[31], the filtering material that resulted in the highest FoM$_{DE}$ was copper.

Symbol	Definition	Ideal Value for Detection of	
		Iodinated Vessel	Calcified Nodule
kVp	Peak x-ray tube voltage	120 kV	120 kV
t_f	Thickness of source filtering	3 mm	3 mm
	Source filtering material	Aluminum	Aluminum
t_t	Thickness of top scintillator	180 µm	161 µm
t_{m-f}	Thickness of metal mid-filter	1040 µm	958 µm
	Metal mid-filter material	Copper	Copper

Table 6.4: Parameters optimized in the analytical model for the conventional single-shot dual-layer imaging system and their ideal values for both of the applications studied.

6.2.3 Comparison Results

Using the found optimized parameters for all three studied DE detector systems, the FoM$_{DE}$ was calculated for both target applications in the I_{ml} and t_c ranges of interest. To validate these results, ray-tracing Monte Carlo simulations were performed for all detector types in their optimized setups using five objects of interest with discrete values of the application parameters that span the entire studied range. From the images obtained, it was possible to combine them to generate a DE enhanced image for each case, and thereby calculate FoM$_{DE}$. The results from these analytical computations and Monte Carlo simulations are shown in Figure 6.5.

The Monte Carlo results clearly follow the same trends as the presented analytical model. This fact corroborates the effectiveness of said model as a first-order optimization method, given that it requires very low computational resources and will provide accurate trends in its results. However, a mean difference of 32 % is observed between the two approaches across all detector types.

Evidently, the imaging system less accurately described by the analytical model is that of the established dual-layer detector. This can be traced to x-ray scattering occurring at the metal mid-filter, an effect that is not accounted for in the developed analytical model but will be considered in the Monte Carlo simulations. A loss of parity between the two

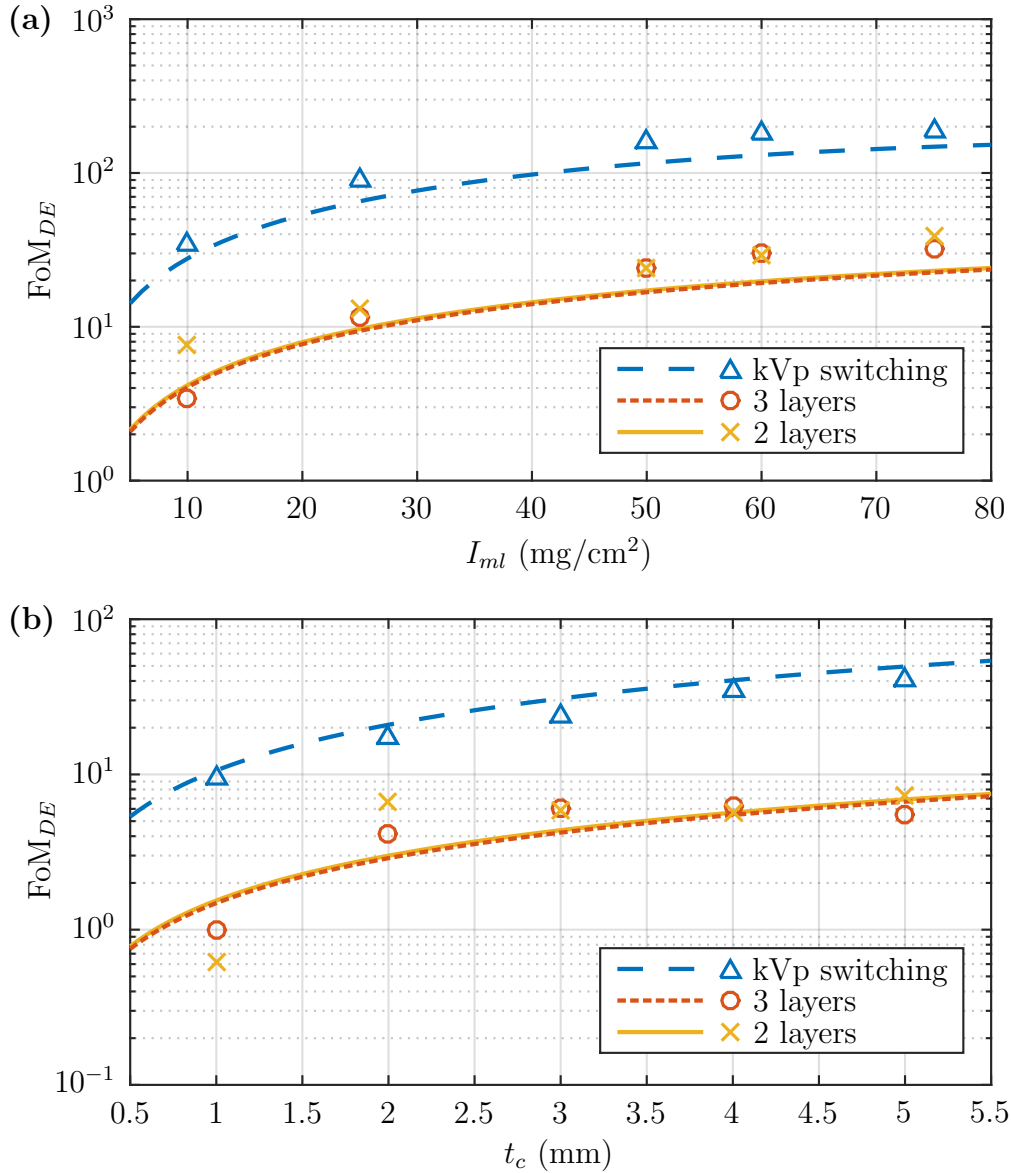**Figure 6.5:** Comparison of optimized FoM$_{DE}$ results for a conventional kVp switching detector, a copper mid-filter single-shot detector (two-layer) and the newly proposed three-layer detector for the **(a)** iodinated vessel visualization and **(b)** calcified nodule detection application. Lines show the analytical model's result, while triangles, crosses and circles show the respective Monte Carlo simulation results.

approaches is therefore expected. Interlayer scattering can also explain disagreements for the proposed three-layer detector, although a metal layer is expected to result in a higher degree of scattering than a FPD. Another notable effect not accounted for in the model are x-ray re-emissions of the scintillating materials, which will slightly modify the x-ray spectra at each layer, leading to diverging FoM_{DE} values between the two approaches.

6.3   Discussion

It is clear from the presented results that the proposed three-layer detector performs comparably to an established single-shot dual-layer detector in its dual-energy imaging capabilities. This fact implies that a detector of the proposed nature is indeed superior to the established single-shot technologies, since the presence of a sensitive middle layer allows it to operate in its conventional radiography mode, and perhaps opens the opportunity for further operational modes and enhanced images at no extra patient exposure. Given these results and the recent decrease in cost of building each flat-panel sensor, the three-layer stacked detector presents a promising alternative to current single-shot imagers with a clear advantage and no performance downsides.

As expected[32, 64], the high spectral separation that can be achieved in kVp switching allowed said system to achieve higher FoM_{DE} results than the proposed detector across the entire studied application parameter range. However, it must be noted that this figure of merit applies only to the detector performances as a DE imager, and does not take into account the high proclivity to motion artifacts of kVp switching imagers. Furthermore, the signal acquired in the middle sensitive layer opens up future potential applications for the proposed detector that might not be possible in these types of imaging systems. Therefore, determining the clear better alternative becomes impossible with the available information. Referring back to Table 2.1, the advantages and disadvantages of each imager type remain the same when selecting the three-layer detector as the best single-shot imager, but with it having the added advantage of creating other types of enhanced images. Choosing the best alternative still depends on the details of the specific application, cost-incurring capabilities, and expertise.

Chapter 7

Conclusion and Future Works

A newly proposed three-layer stacked flat-panel detector for two specific applications in multi-spectral medical imaging was investigated, and its performance as a dual-energy imager was optimized within practical limitations. When comparing this optimal performance with established dual-layer detectors, this proposed detector becomes the clear better alternative for single-shot imagers since it performed similarly as a DE imager but has the added capability of simultaneously obtaining conventional radiography images. It also becomes a more compelling alternative to kVp switching systems, since it shares all the advantages with other single-shot imagers and adds the signal of the middle layer.

It is possible to build on the work presented in this thesis and expand further on the potential of the three-layer stacked detector. First, the work presented here focused on DE detector optimization according to a particular chosen figure of merit. Perhaps the largest issue with this figure is that it will benefit from individual image blurring, as it is based on the variance of the signal at certain regions. The noise associated with each signal will therefore decrease as a consequence of blurring. However, blurring can have adverse effects on the detectability of certain objects, especially for very thick scintillators and large signal spreads. To account for this, the optimization and comparison procedure detailed here could be repeated while considering other figures of merit that better describe the possible adverse effects of blurring. To do so, these figures must take into account the loss in spacial frequency resolution due to blurring and thus must describe the frequency response of the system. Likely candidates of this type of metrics include the modulation transfer function, the noise equivalent quanta, and the detective quantum efficiency[65, 66].

Next, I see great potential in optimizing other possible imaging system characteristics, especially if full control over the type of x-ray source used is assumed. The simplest new pathway that could be investigated is testing other anode materials aside from tungsten, including rhodium and molybdenum, which might provide a more optimal spectrum for a particular application. A more interesting possibility is the use of either two individual sources set at different kVp values or a multiple-anode source. The superposition of multiple spectra in the incoming x-ray beam could provide the higher spectral separation needed to improve single-shot imaging results.

Lastly, and perhaps more interestingly, further operational modes for the detector that better make use of the image obtained in the middle layer of the detector should be investigated. This newly available information has never been present in single-shot detectors before, and hence the potential uses are plentiful. Likely candidates that I see as great examples of this are creating false color radiographic images in which the signal from each detector layer is somehow mapped to one of the RGB channels, or expanding material decomposition methods of object enhancement to include the information from this third image.

References

[1] Rebecca Smith-Bindman, Diana L. Miglioretti, and Eric B. Larson. Rising use of diagnostic medical imaging in a large integrated health system. *Health Affairs*, 27(6):1491–1502, 2008.

[2] William R. Hendee, E. Russell Ritenour, and Kenneth R. Hoffmann. *Medical Imaging Physics, Fourth Edition*, volume 30. Wiley-Liss, 4th edition, 2003.

[3] Jerrold T. Bushberg, J. Anthony Seibert, Edwin M. Leidholdt, John M. Boone, and Edward J. Goldschmidt. *The Essential Physics of Medical Imaging*, volume 30. Wolters Kluwer, 3rd edition, 2003.

[4] Jens Als-Nielsen and Des McMorrow. *Elements of Modern X-ray Physics*. Wiley, 2nd edition, 2011.

[5] A. a. Bharath. *Introductory Medical Imaging*, volume 3. Morgan & Claypool Publishers, 1st edition, 2008.

[6] Glenn F. Knoll. *Radiation Detection and Measurement*, volume 3. Wiley, 4th edition, 2010.

[7] M.J. Berger, J.H. Hubbell, S.M. Seltzer, J. Chang, J.S. Coursey, R. Sukumar, D.S. Zucker, and K. Olsen. *XCOM: Photon cross sections database*. The National Institute of Standards and Technology (NIST), 1987.

[8] John Rowlands and John Yorkston. Flat Panel Detectors for Digital Radiography. In *Handbook of Medical Imaging, Volume 1. Physics and Psychophysics*, chapter 4, pages 223–328. SPIE, 1000 20th Street, Bellingham, WA 98227-0010 USA, 2000.

[9] SO Kasap and JA Rowlands. Direct-conversion flat-panel X-ray image detectors. *IEE Proceedings-Circuits, Devices and Systems*, 2002.

[10] J a Rowlands and K W Taylor. Absorption and noise in cesium iodide x-ray image intensifiers. *Medical physics*, 10(6):786–795, 1983.

[11] G. T. Barnes. Noise analysis of radiographic imaging. In K. Doi, L. Lanzl, and P. J. P. Lin, editors, *Recent Advances in Digital Imaging, Proceedings of the 1984 AAPM Summer School*, pages 16–38. American Institute of Physics, Woodbury, NY, 1985.

[12] Aldo Badano. Optical blur and collection efficiency in columnar phosphors for X-ray imaging. *Nuclear Instruments and Methods in Physics Research, Section A: Accelerators, Spectrometers, Detectors and Associated Equipment*, 508(3):467–479, 2003.

[13] V V Nagarkar, T K Gupta, S R Miller, Y Klugerman, M R Squillante, G Entine, and A Overview. Structured CsI (Tl) Scintillators for X-ray Imaging Applications B . Structured X-ray Imaging Scintillators. *Imaging*, 45(3):1–5, 1998.

[14] Stuart R. Miller, Valeriy Gaysinskiy, Irina Shestakova, and Vivek V. Nagarkar. Recent Advances in Columnar CsI(Tl) Scintillator Screens. *Proceedings of SPIE*, 5923:59230F1–59230F10, 2005.

[15] ALN Stevels and AD Schramad. Vapor-Deposited CsI:Na Layer II Screens for Applications in X-ray Imaging Devices. *Philips Research Reports*, 29(4):353–362, 1974.

[16] Melanie Freed, Subok Park, and Aldo Badano. A fast, angle-dependent, analytical model of CsI detector response for optimization of 3D x-ray breast imaging systems. *Medical Physics*, 37(6):2593–2605, jun 2010.

[17] Tianhu Lei and Jayaram K. Udupa. Statistical properties of x-ray CT and MRI: from imaging physics to image statistics. volume 4682, pages 82–93, may 2002.

[18] Daniel Rimkus and Norman A Baily. Quantum noise in detectors. *Med. Phys.*, 10(4):470–471, 1983.

[19] Sheldon M Ross. *Introduction to Probability and Statistics for Engineers and Scientists, Fourth Edition*. Academic Press, 2009.

[20] Robert E Alvarez and Albert Macovski. Energy-selective reconstructions in X-ray computerized tomography. *Physics in medicine and biology*, 21(5):733–744, 1976.

[21] J.H. Hubbell and S.M. Seltzer. Tables of x-ray mass attenuation coefficients and mass energy-absorption coefficients (version 1.4), 2004.

[22] Robert E Alvarez. *Extraction of Energy-Dependent Information in Radiography*. PhD thesis, Stanford University, 1976.

[23] Samuel Richard and Jeffrey H. Siewerdsen. Cascaded systems analysis of noise reduction algorithms in dual-energy imaging. *Medical Physics*, 35(2):586–601, 2008.

[24] Jesse Tanguay, Ho Kyung Kim, and Ian a. Cunningham. A theoretical comparison of x-ray angiographic image quality using energy-dependent and conventional subtraction methods. *Medical Physics*, 39(2012):132, 2012.

[25] Peter Vock and Zsolt Szucs-Farkas. Dual energy subtraction: Principles and clinical applications. *European Journal of Radiology*, 72:231–237, 2009.

[26] Adam S Wang, Scott S Hsieh, and Norbert J Pelc. A Review of Dual Energy CT : Principles , Applications , and Future Outlook. *CT Theory and Applications*, 21(3):367–386, 2012.

[27] Heber MacMahon, Feng Li, Roger Engelmann, Rachael Roberts, and Samuel Armato. Dual energy subtraction and temporal subtraction chest radiography. *Journal of thoracic imaging*, 23(2):77–85, 2008.

[28] G T Barnes, R A Sones, M M Tesic, D R Morgan, and J N Sanders. Detector for dual-energy digital radiography. *Radiology*, 156(2):537–540, aug 1985.

[29] T. Ishigaki, S. Sakuma, Y. Horikawa, M. Ikeda, and H. Yamaguchi. One-shot dual-energy subtraction imaging. *Radiology*, 161(1):271–273, 1986.

[30] Nicholas Allec, Shiva Abbaszadeh, Andre Fleck, Olivier Tousignant, and Karim S. Karim. K-edge imaging using dual-layer and single-layer large area flat panel imagers. *IEEE Transactions on Nuclear Science*, 59(5 PART 1):1856–1861, 2012.

[31] Jong Chul Han, Ho Kyung Kim, Dong Woon Kim, Seungman Yun, Hanbean Youn, Soohwa Kam, Jesse Tanguay, and Ian a. Cunningham. Single-shot dual-energy x-ray imaging with a flat-panel sandwich detector for preclinical imaging. *Current Applied Physics*, 14(12):1734–1742, 2014.

[32] Robert E Alvarez, J Anthony Seibert, and Stephen K Thompson. Comparison of dual energy detector system performance. *Medical physics*, 31(2004):556–565, 2004.

[33] Ian Alexander Cunningham, M. S. Westmore, and A. Fenster. A spatial-frequency dependent quantum accounting diagram and detective quantum efficiency model of signal and noise propagation in cascaded imaging systems. *Medical Physics*, 21(3):417–427, 1994.

[34] L a Lehmann, R E Alvarez, a Macovski, W R Brody, N J Pelc, S J Riederer, and a L Hall. Generalized image combinations in dual KVP digital radiography. *Medical physics*, 8(5):659–667, 2006.

[35] Richard J. Warp and James T. Dobbins. Quantitative evaluation of noise reduction strategies in dual-energy imaging. *Medical physics*, 30(2):190–8, 2003.

[36] Nicholas Allec and Karim S. Karim. Multilayer x-ray detector for contrast-enhanced digital subtraction mammography. *Physics*, 7622:76221M–76221M–12, 2010.

[37] Thomas M. Bashore, Stephen Balter, Ana Barac, John G. Byrne, Jeffrey J. Cavendish, Charles E. Chambers, James Bernard Hermiller, Scott Kinlay, Joel S. Landzberg, Warren K. Laskey, Charles R. McKay, Julie M. Miller, David J. Moliterno, John W.M. Moore, Sandra M. Oliver-McNeil, Jeffrey J. Popma, and Carl L. Tommaso. 2012 American College of Cardiology Foundation/Society for Cardiovascular Angiography and Interventions Expert Consensus Document on Cardiac Catheterization Laboratory Standards Update. *Journal of the American College of Cardiology*, 59(24):2221–2305, 2012.

[38] Georgios Sianos, Marie-Angèle Morel, Arie Pieter Kappetein, Marie-Claude Morice, Antonio Colombo, Keith Dawkins, Marcel van den Brand, Nic Van Dyck, Mary E Russell, Friedrich W Mohr, and Patrick W Serruys. The SYNTAX Score: an angiographic tool grading the complexity of coronary artery disease. *EuroIntervention*, 1(2):219–227, 2005.

[39] Richard S. Fraser, Nestor L. Muller, Neil C. Colman, and P. D. Pare. *Diagnosis of Diseases of the Chest.* Saunders, 4 edition edition, 1999.

[40] William G Berger, William K Erly, Elizabeth a Krupinski, James R Standen, and Robert G Stern. The Solitary Pulmonary Nodule on Chest Radiography. *American Journal of Roentgenology*, 176(1):201–204, jan 2001.

[41] H Page McAdams, Ehsan Samei, James Dobbins, Georgia D Tourassi, and Carl E Ravin. Recent advances in chest radiography. *Radiology*, 241(3):663–683, 2006.

[42] F. Kelcz, F. E. Zink, W. W. Peppler, D. G. Kruger, D. L. Ergun, and C. A. Mistretta. Conventional chest radiography vs dual-energy computed radiography in the detection and characterization of pulmonary nodules. *American Journal of Roentgenology*, 162(2):271–278, 1994.

[43] Albert Macovski. *Medical Imaging Systems.* 1983.

[44] C. W E Van Eijk. Inorganic scintillators in medical imaging detectors. *Nuclear Instruments and Methods in Physics Research, Section A: Accelerators, Spectrometers, Detectors and Associated Equipment*, 509:17–25, 2003.

[45] Wei Zhao, Goran Ristic, and J a Rowlands. X-ray imaging performance of structured cesium iodide scintillators. *Medical physics*, 31(9):2594–2605, 2004.

[46] Robert K. Swank. Absorption and noise in x-ray phosphors. *Journal of Applied Physics*, 44(9):4199, 1973.

[47] W Yao and J B Farr. Derivation of Residual Noise of Filtered Poisson and Gaussian Series. In *World Congress on Medical Physics and Biomedical Engineering*, volume 27, pages 207–210. 2015.

[48] R a Sones and G T Barnes. Noise correlations in images acquired simultaneously with a dual-energy sandwich detector. *Medical physics*, 16(6):858–861, 1989.

[49] Seong Ho Park, Jin Mo Goo, and Chan-Hee Jo. Receiver operating characteristic (ROC) curve: practical review for radiologists. *Korean Journal of Radiology*, 5(March):11–8, 2004.

[50] Iii Dobbins, James T. Image Quality Metrics for Digital Systems. *Handbook of Medical Imaging*, pages 161–221, 2000.

[51] Jesse Evan Tanguay and Ian Cunningham. *Image quality of energy-dependent approaches for x-ray angiography.* PhD thesis, 2013.

[52] D M Gauntt and G T Barnes. X-ray tube potential, filtration, and detector considerations in dual-energy chest radiography. *Medical physics*, 21(2):203–218, 1994.

[53] Paolo Russo. Physical basis of x-ray imaging. In Anders Brahme, editor, *Comprehensive Biomedical Physics*, chapter 2.01, pages 1–14. Elsevier Science Limited, 2014.

[54] Christiane S. Burton, John R. Mayo, and I. a. Cunningham. Theoretical and experimental comparison of image signal and noise for dual-energy subtraction angiography and conventional x-ray angiography. 9412:941219, 2015.

[55] I a Cunningham, S Yamada, B B Hobbs, and a Fenster. Arterial flow characterization with a photodiode array based imaging system. *Medical physics*, 16(2):179–187, 1989.

[56] J H Siewerdsen, a M Waese, D J Moseley, S Richard, and D a Jaffray. Spektr: a computational tool for x-ray spectral analysis and imaging system optimization. *Medical physics*, 31(2004):3057–3067, 2004.

[57] J M Boone and J a Seibert. An accurate method for computer-generating tungsten anode x-ray spectra from 30 to 140 kV. *Medical physics*, 24(1997):1661–1670, 1997.

[58] M R Ay, S Sarkar, M Shahriari, D Sardari, and H Zaidi. Assessment of different computational models for generation of x-ray spectra in diagnostic radiology and mammography. *Medical physics*, 32(2005):1660–1675, 2005.

[59] Diksha Sharma, Andreu Badal, and Aldo Badano. hybridMANTIS: a CPU-GPU Monte Carlo method for modeling indirect x-ray detectors with columnar scintillators. *Physics in Medicine and Biology*, 57:2357–2372, 2012.

[60] Aldo Badano and Josep Sempau. MANTIS: combined x-ray, electron and optical Monte Carlo simulations of indirect radiation imaging systems. *Physics in medicine and biology*, 51:1545–1561, 2006.

[61] F Salvat, J Fernández-Varea, and J Sempau. PENELOPE-2006: A code system for Monte Carlo simulation of electron and photon transport. *Nuclear Energy Agency*, 2006.

[62] M.J. Berger, J.S. Coursey, M.A. Zucker, and J. Chang. Stopping-power and range tables for electrons, protons, and helium ions, 1998.

[63] National Center for Biotechnology Information. PubChem Compound Database: Iopromide Compound Summary, 2005.

[64] S Richard and J H Siewerdsen. Optimization of dual-energy imaging systems using generalized NEQ and imaging task. *Medical physics*, 34(2007):127–139, 2007.

[65] H H Barrett and K J Myers. Foundations of Image Science John Wiley & Sons. *Inc., Hoboken, NJ*, 2004.

[66] Rm Nishikawa. The Fundamentals of MTF, Wiener Spectra, and DQE. *Annual Meeting of the American Association of Physicists in Medicine*, 1999.